JOURNAL OF GEOPHYSICAL RESEARCH, VOL. 104, NO. D13, PAGES 16,327–16,348, JULY 20, 1999

Middle Atmosphere High Resolution Spectrograph Investigation

Robert R. Conway,[1] Michael H. Stevens,[1] Charles M. Brown,[1]
Joel G. Cardon,[2] Scott E. Zasadil,[3] and George H. Mount[4]

Abstract. The Middle Atmosphere High Resolution Spectrograph Investigation (MAHRSI) was developed specifically to measure the vertical density profiles of hydroxyl (OH) and nitric oxide (NO) in the middle atmosphere from space. MAHRSI was launched on its first flight in November 1994 on the CRISTA-SPAS satellite that was deployed and retrieved by the space shuttle. The instrument measured the radiance profiles of ultraviolet solar resonance fluorescence on the Earth's limb with a spectral resolving power of 15,600 at a wavelength of 308 nm and 7200 at 215 nm. The instantaneous height of the field of view projected to the tangent point was about 300 m. OH limb radiance measurements were made between altitudes of 90 and 30 km, and each limb scan extended over a horizontal distance of 1200 km. For NO a limb scan extended between altitudes of 140 and 76 km and over a horizontal distance 700 km. Observations were made from 52°S latitude to 62°N latitude. The OH measurements have been inverted to provide the first global maps of the vertical distribution of OH between 90 and 50 km. The data show a detailed history of the morning formation of a strongly peaked layer of OH at an altitude of 68 km. This layer was produced by solar photodissociation of a thin layer of water vapor peaked at 65 km extending between 30°S and 35°N observed contemporaneously by the Halogen Occultation Experiment (HALOE) on the Upper Atmosphere Research Satellite. MAHRSI was successfully flown for a second time in August 1997 under conditions that extended the geographical coverage to 72°N latitude and local solar time coverage through the afternoon hours. This paper provides a detailed description of the experiment and instrumentation, of the algorithms used to reduce the spectral data and perform the inversions, and presents examples of key results from the 1994 flight.

1. Introduction

It has been nearly 50 years since *Bates and Nicolet* [1950] investigated the implications of the presence of hydrogen atoms and hydroxyl radicals produced by the dissociation of water vapor by solar Lyman α radiation in the mesosphere. Atmospheric measurements and the theoretical understanding of the role of the odd hydrogen chemical family (H + OH + HO_2) in atmospheric chemistry have expanded dramatically during those years as demonstrated by the results of recent stratospheric aircraft campaigns [*Cohen et al*., 1994; *Salawitch et al*., 1994; *Wennberg et al*., 1994a]. Today it is clear that despite its presence in trace amounts with mixing ratios of only parts per trillion or billion by volume, the OH radical has a pervasive influence on the photochemistry of the atmosphere from the boundary layer to the homopause [*Thompson*, 1992; *Mount and Williams*, 1997].

Measurements of OH have been sparse in every atmospheric region. Most experiments have sought to exploit the large absorption band strengths of the $A^2\Sigma^+$–$X^2\Pi(v', 0)$ progression in the ultraviolet (UV). *Anderson* [1971] observed the vertical column emission rate of the solar resonance fluorescence (0, 0) band at 308 nm with a spectrometer viewing the zenith from a rocket at twilight. For more than 20 years that measurement remained the only detection of OH in the mesosphere. An extensive body of ground-based measurements of the vertical column of OH using the extinction of sunlight in the (0, 0) band have been carried out at several locations around the globe and are reported by C. R. Burnett and coworkers [e.g., *Wood et al*., 1994]. Stratospheric air sampling experiments using laser-induced fluorescence of the (0, 0) band have flown successfully on balloons and high-altitude aircraft [*Stimpfle et al*., 1990; *Wennberg et al*., 1994b; *Brune et al*., 1998]. *Heaps and McGee* [1985] report a series of balloon-borne lidar measurements that also used fluorescence of the (0, 0) band, and *Morgan et al*. [1993] report a limb scan observation of (0, 0) band solar fluorescence in the mesosphere from the space shuttle orbiter bay. Balloon and aircraft measurements of OH in the stratosphere using the rotation transitions at 84 and 100 μm are reported by *Carli et al*. [1989], *Pickett and Peterson* [1996], and *Johnson et al*. [1995]. *Titz et al*. [1995] have reported 2.5 THz heterodyne observations by an aircraft experiment, and it is this technique which will be utilized by the Microwave Limb Sounder experiment (EOS MLS) currently under development for the Earth Observing System CHEM satellite platform scheduled for launch in late 2002 [*Waters*, 1997].

Since 1964, ultraviolet solar resonance fluorescence has also been used successfully to measure the distribution of nitric oxide (NO) in the thermosphere from both rockets and satellites [*Siskind and Rusch*, 1992, and references therein; *Siskind*

[1]E. O. Hulburt Center for Space Research, Naval Research Laboratory, Washington, D. C.
[2]Computational Physics, Inc., Fairfax, Virginia.
[3]Union Switch & Signal, Inc., Pittsburgh, Pennsylvania.
[4]Department of Civil and Environmental Engineering, Washington State University, Pullman.

Paper number 1998JD100036.
0148-0227/99/1998JD100036$09.00

et al., 1998]. The production of NO in the thermosphere is photochemically controlled through the dissociation of N_2 by both photoelectrons and precipitating auroral particles. Its abundance responds to solar activity at low latitudes and to geomagnetic activity at high latitudes. In the mesosphere, where it becomes long-lived, the global circulation increasingly controls its distribution. NO also participates in the heating and cooling of the lower thermosphere and mesosphere through the 5.3 μm band emission. Because NO responds to most of the physical processes that couple the thermosphere and mesosphere, synoptic observations provide a rigorous test of photochemical transport models of this altitude region. Since 1991, the Halogen Occultation Experiment (HALOE) on the Upper Atmosphere Research Satellite (UARS) has measured the NO distribution from the lower thermosphere into the stratosphere using the solar occultation technique in the infrared [*Russell et al*., 1993].

To address the serious lack of global OH observations, the MAHRSI experiment was flown on board the CRISTA-SPAS satellite that was deployed by the shuttle orbiter for 8 days of free flight [*Offermann and Conway*, 1995] during the ATLAS 3/CRISTA-SPAS/Shuttle Solar Backscatter Ultraviolet (SSBUV) STS 66 space shuttle mission in November 1994. MAHRSI is an ultraviolet spectrograph experiment whose objectives were (1) to measure the vertical distribution and diurnal variation of OH in the mesosphere and upper stratosphere on a global scale with sufficient accuracy, precision, and time resolution to test the current understanding of mesospheric HO_x chemistry, and (2) to measure the vertical distribution of NO in the lower thermosphere and upper mesosphere to provide synoptic global maps for use in quantifying the coupling of these regions on short timescales. During the flight, MAHRSI successfully acquired the first global maps of the vertical distribution of OH in the middle atmosphere. *Conway et al*. [1996] reported preliminary OH results. These data corroborate the presence of a layer of H_2O in the mesosphere between the altitudes of 65 and 70 km where mixing ratios as high as 8 ppmv are observed by HALOE. As discussed by *Summers et al*. [1997] (hereinafter referred to as SUM97), the presence of this layer cannot be explained by the conventional theory of the photochemistry and transport of H_2O through the middle atmosphere. MAHRSI NO measurements provided a 7.5 hour snapshot of the vertical distribution of NO in the lower thermosphere and mesosphere during low solar activity but immediately following a period of high geomagnetic activity. *Stevens et al*. [1997] presented these data and showed that the vertical profiles of NO were highly structured and variable on short timescales and/or spatial scales and are suggestive of complex dynamical control.

This paper presents a detailed description of the MAHRSI experiment, the characterization and calibration of the instrument in the laboratory, the processing of the flight data, and reports a summary of new results for OH. Section 2 describes the measurement approach, section 3 discusses the flight operations and resulting geographic coverage, while section 4 covers the instrument design, its performance, and the conversion of the raw data to radiance profiles. The inversion algorithm used to infer number density profiles is described in section 5, and section 6 presents the results. A comparison of the scientific results with model predictions and discussion of implications for our understanding of the mesosphere are presented by *Summers et al*. [1996, 1997].

2. Measurement Approach

2.1. Experiment Overview

MAHRSI was designed specifically to measure OH and NO from space. Measurement of limb intensity profiles of their ultraviolet solar resonance fluorescence in the altitude region from 30 to 140 km provided high vertical resolution and sufficient time and horizontal resolution to characterize in detail their global distribution. The CRISTA-SPAS satellite was developed for the German Aerospace Center (DLR) by the Daimler Benz Aerospace Corporation (DASA). MAHRSI was integrated with the satellite along with the Cryogenic Infrared Spectrometers and Telescopes for the Atmosphere (CRISTA) [*Offermann et al*., this issue] for a joint atmospheric chemistry and dynamics campaign. CRISTA-SPAS was deployed by the crew of the space shuttle Atlantis on November 4, 1994, retrieved 8 days later, and returned to Kennedy Space Center. The experiment geometry is shown in Figure 1. Throughout the limb observations, the CRISTA-SPAS spacecraft maintained a stable attitude with respect to the local vertical and local horizontal with sufficient accuracy that random errors in the tangent height were less than 250 m including the eccentricity of the orbit and the shape of the geoid. For a tangent height of 68 km the instantaneous projected dimensions of the $0.01° \times 1.15°$ field of view at the tangent point were 0.3 km high by 34.4 km wide. Vertical scans of the sunlit atmosphere were obtained by stepping the field of view with a scanning mirror downward through a range of tangent heights while the spacecraft moved along its orbit. Each complete scan required 151 s for OH and 88 s for NO. The total integration time at each altitude step during the scan varied from 2.2 s to 6.6 s depending on the observing mode. For this "bright limb" geometry the observed slant intensity at each step is generally dominated by emission from the altitude region near the tangent height. Vertical density profiles were derived from the measurements by computationally inverting the slant intensity scans to infer the number density (molecules cm^{-3}) of the fluorescing gas at the tangent point. The distance traveled by the spacecraft during a single altitude scan determined the horizontal resolution of the observations, and this generally varied from 1200 km for OH to 500 km for NO. Since the orbital period was about 90 min, 24 hours and 16 sequential orbits of observations provided complete longitudinal coverage.

2.2. Solar Resonance Fluorescence

MAHRSI observed the solar resonance fluorescence OH $A^2\Sigma^+$–$X^2\Pi$ (0, 0) band in the wavelength region near 308 nm and the NO $A^2\Sigma^+$–$X^2\Pi$ (1, 0) band near 215 nm. The basic equation describing the experiment is

$$I(\lambda, \mathbf{r}, \hat{n}) = \int \frac{g(\lambda, \mathbf{r}')\rho(\mathbf{r}')Q(\mathbf{r}')}{4\pi} e^{-\tau(\lambda)}\, ds, \qquad (1)$$

where I (photon $cm^{-2}\ s^{-1}\ nm^{-1}\ sr^{-1}$) is the spectral radiance of the fluorescence at wavelength λ, $\mathbf{r}$ is the satellite position vector, $\mathbf{r}'$ is the position vector to the fluorescing volume, and $\hat{n}$ specifies the viewing direction. The fluorescence emission rate factor g, or g factor, is the number of photons scattered per second per molecule. ρ (cm^{-3}) is the number density of the ground state molecules, Q is the emission efficiency which accounts for the effects of collisional deactivation of the various vibrational levels of the excited electronic state, and $\tau(\lambda)$ is the absorption optical depth along the line of sight path from

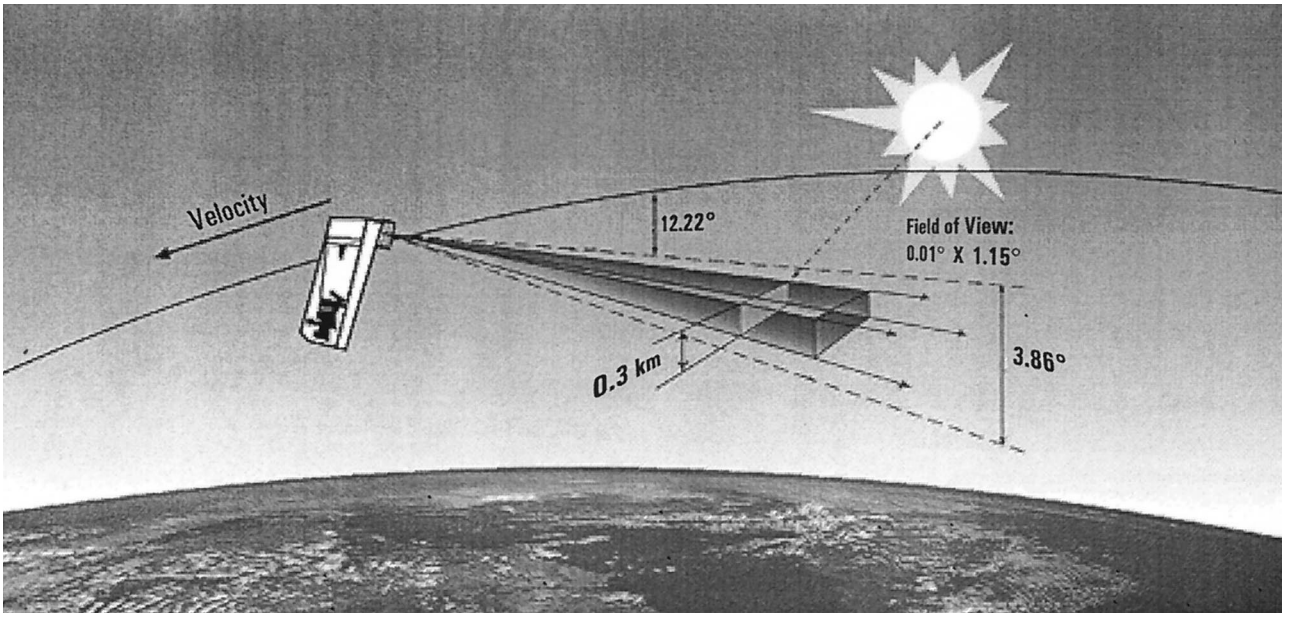

Figure 1. Experiment geometry. For a tangent height of 68 km the dimensions of the field of view projected to the tangent point was 0.3 km high and 34.4 km wide. The actual angular scan range for OH and NO varied depending on the observing mode. The scan durations were 151 s for OH and 88 s for NO.

the emitting volume to the instrument. The computation of the g factor for a fluorescence band requires the careful evaluation of all possible electronic transitions populating the upper level of each rotational line during the absorption of solar photons, and of the distribution of emission probability among all possible downward radiative transitions. The detailed calculations used in the analysis of the MAHRSI observations are described by *Stevens* [1995] for NO and *Stevens and Conway* [this issue] for OH.

2.2.1. Rayleigh scattering background. For both OH and NO the detection of solar fluorescence in the middle atmosphere is severely affected by the bright radiation field produced from Rayleigh scattering of sunlight by N_2 and O_2. The Rayleigh-scattered solar spectrum forms a spectrally complex background that must be identified and subtracted from each observation. MAHRSI used high spectral resolution to resolve the fluorescence bands and separate them from the background. This was particularly effective for OH observations where the spectral resolution of 0.02 nm (resolving power of 15,600) was sufficient to resolve discrete features composed of individual rotational emission lines in the A–X (0, 0) band near the wavelength of 308 nm. Plate 1 illustrates the separation of the Rayleigh-scattering spectrum from the OH spectrum. The upper panel compares the spectrum measured at a tangent height of 70 km (solid black curve) with the estimated contribution from Rayleigh scattering (blue dashed curve). As shown in the lower panel, the OH spectrum is apparent in the residual (black solid curve) formed by subtracting the Rayleigh spectrum from the total airglow spectrum. The dashed red curve is the theoretical OH spectrum scaled in magnitude to best fit the data. At 70 km, in the center core of the OH features, the OH emission is about 40% of the total (fluorescence plus Rayleigh) signal, but at 40 km the Rayleigh scattering becomes 30 times brighter, while the OH slant intensity increases by about a factor of only 2 or 3. Thus at the lowest altitudes the OH fluorescence lines are only a few percent of the total signal at line center.

2.2.2. Effects of collisional deactivation and ozone absorption. As stated explicitly in (1), the relation of the observed spectral radiance to the number density of ground state molecules is dependent on the emission efficiency Q and the extinction optical depth. Laboratory measurements indicate that the OH $A^2\Sigma$ state is efficiently deactivated by collisions with N_2 and O_2. The collisions modify the population of the $v' = 0$ vibrational level from its purely radiative value both by deactivation and by induced relaxation of the $v' = 1$ level, which is itself excited by absorption of sunlight.

Both Rayleigh scattering and O_3 absorption contribute to the extinction optical depth. O_3 also is important in the g factor calculation for both OH (0, 0) and (1, 0) bands due to extinction of the solar beam. Therefore the retrieval of OH in the upper stratosphere is sensitive to the laboratory-measured collisional deactivation rates and to the amount of O_3 in the observed slant column. Section 6 discusses these issues in more detail.

3. Flight Operations, Geographic, and Local Time Coverage

The space shuttle Atlantis was launched from Kennedy Space Center on the STS 66 mission November 3, 1994, at 1159 LT or UT day 307/1659. Nineteen hours and 50 min later, CRISTA-SPAS was released for 8 days of free flight. MAHRSI began observations at 308/1430 and was powered off at 316/1130. The circular orbit had an altitude of 304 km and an inclination of 57°. During atmospheric operations the Astro-Shuttle Pallet Satellite (ASTRO-SPAS) cold gas (He) attitude control system held the spacecraft stable in the Local Vertical Local Horizontal (LVLH) reference frame. Orbital state vectors were generated continuously by an onboard Global Positioning System (GPS) receiver and were used together with a model of the geoid to point the reference line of sight vector in the antivelocity direction, 18° above the orbital plane, and at a constant tangent height above the geoid. This attitude placed

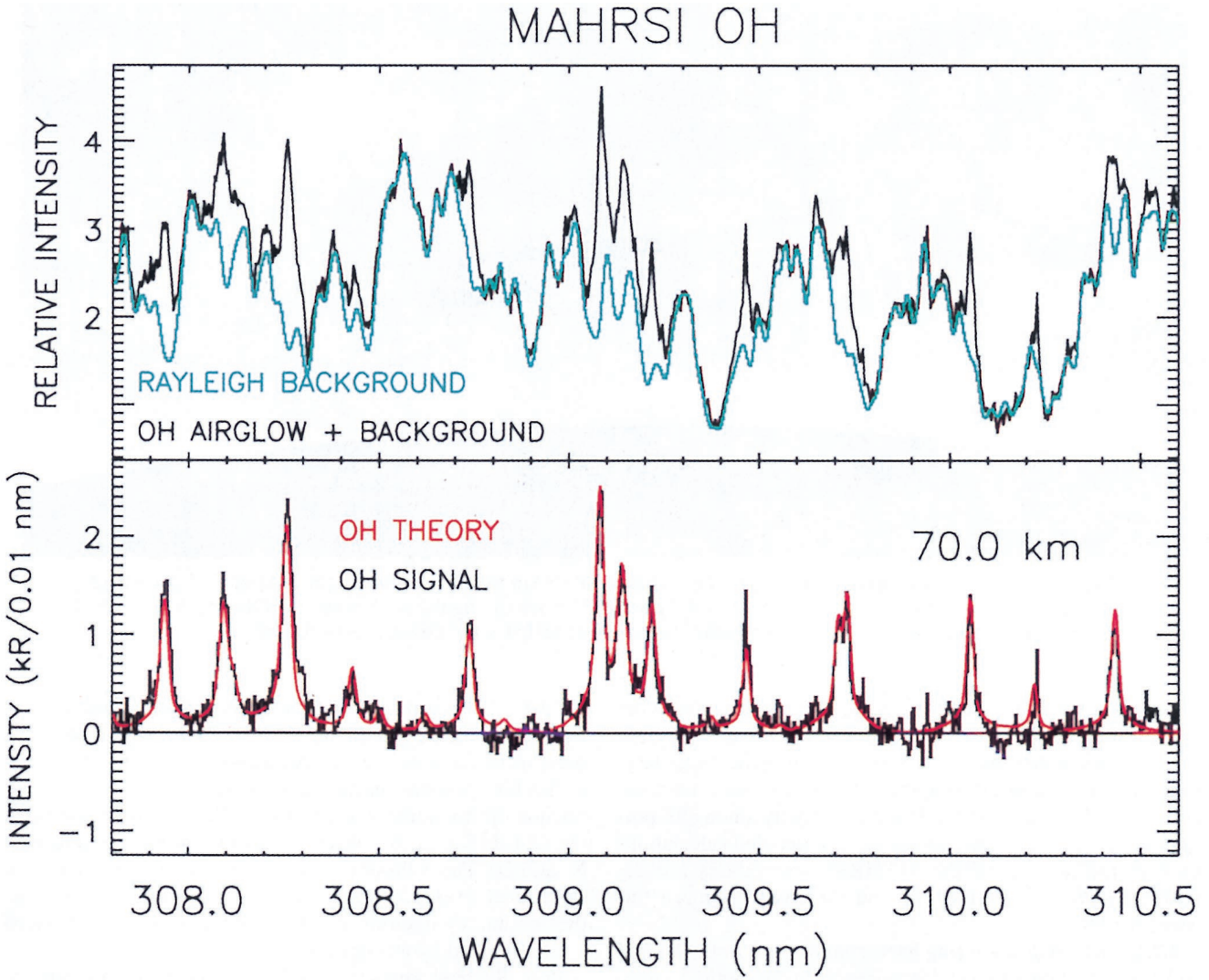

Plate 1. Retrieval of the fluorescence spectrum of OH from the observation at a tangent height of 70 km. The black curve in the upper panel is the total airglow signal, and the overlying blue curve is the estimated contribution of Rayleigh scattering by N_2 and O_2. The black curve in the lower panel is the residual computed by subtracting the Rayleigh-scattering contribution from the total, and the red curve is the theoretical OH spectrum convolved with the instrument spectral resolution function and normalized to the data.

the observed tangent point west of the subsatellite point at the ascending node. Deviations from the desired tangent height during a typical 24-hour period were ± 0.25 km. The alignment error of the MAHRSI line of sight with respect to the spacecraft reference vector was measured before launch and verified on orbit by observing the star α Canis Majoris with the instrument. As a result, all scan angles (measured from the local horizontal) were reduced by 5 arc min. A second observation of α C Ma at the end of the mission found the alignment offset unchanged.

During the flight the status of the instrument was continuously monitored, and a snapshot of the science data was relayed in real time to the payload ground support equipment using the orbiter telemetry downlink. All commands to the instrument were transmitted from the ASTRO-SPAS ground operations center.

MAHRSI's measurements of OH and NO are restricted to the sunlit atmosphere, and during orbit nights the instrument was normally placed in an idle mode to conserve power. OH is primarily produced by photolytic processes and suffers strong diurnal variations, so local solar time (LST) is an important parameter in modeling its distribution in the middle atmosphere. The geographic and local solar time coverage of the observations were determined by the launch time and day of year, the inclination of the orbit, and the fixed attitude of the spacecraft. The attitude of the spacecraft (with the line of sight 18° from the orbital plane) produced a uniform geographic coverage that was highly effective for producing global maps. The inclination of the orbit limited the range of observed latitudes to 52°S to 62°N. In general, MAHRSI observed the morning terminator near 50°S, crossed the equator moving north at about 0930 LST, and observed the evening terminator shortly after turning south from 62°N. This coverage is depicted in Figure 2. Because the middle atmosphere is optically thick to the solar UV energy responsible for the photolysis of H_2O and O_3, the distribution of OH is also sensitive to solar zenith angle (SZA). The distribution of SZAs for these observations was influenced by the regression of the orbit and the

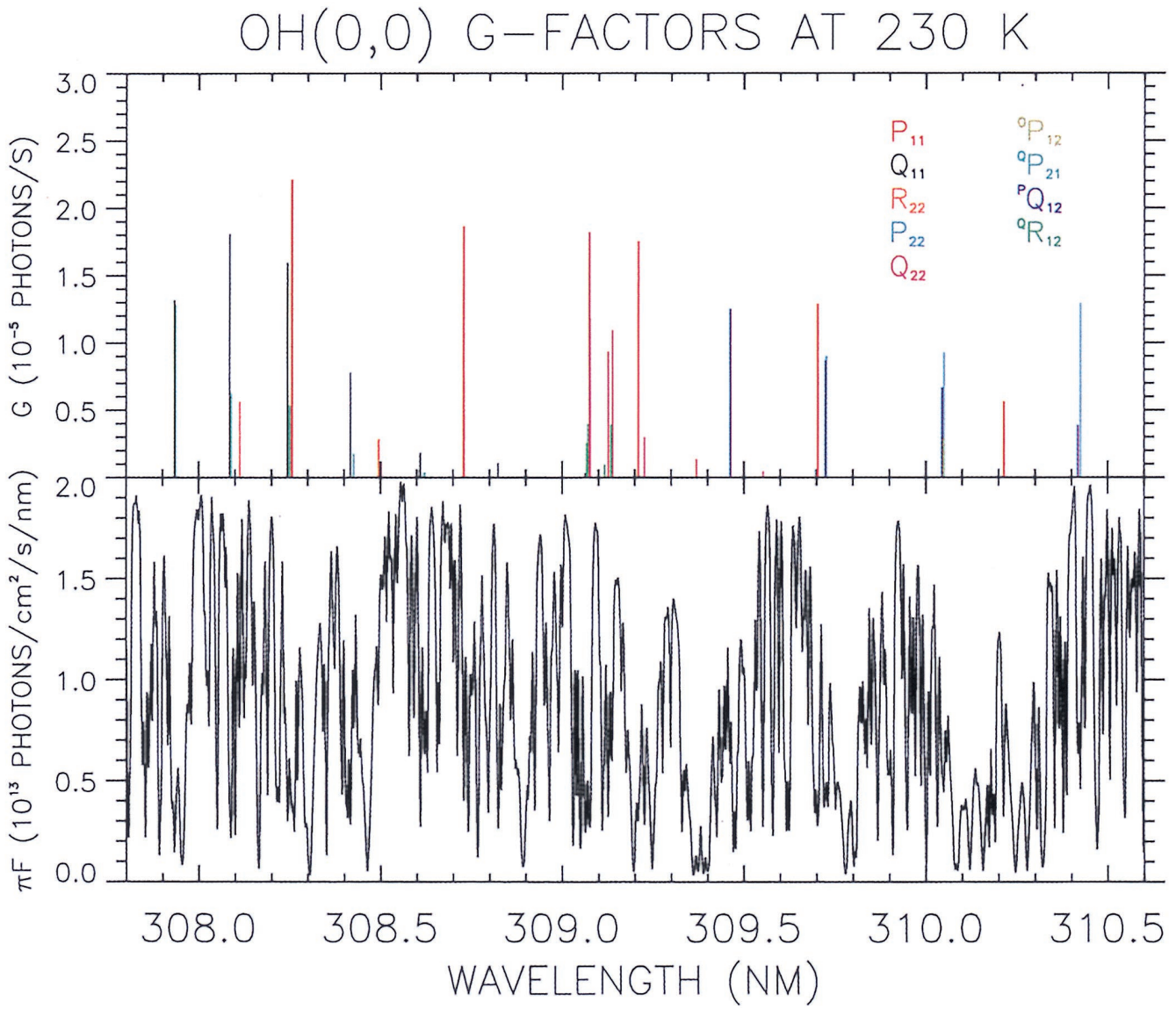

Plate 2. Rotational line locations and fluorescence g factors for the OH spectrum are shown in the upper panel, and the exciting solar Fraunhofer spectrum in the same spectral region is shown in the lower panel.

resulting changes in the β angle, the angle between the orbit plane and the vector to the Sun. This angle, which is equal to the minimum SZA observed at the spacecraft during any orbit, was $-28°$ at launch but increased to $-68°$ on the final orbit. The SZA at the tangent point was further increased by the fact that at all times MAHRSI looked away from the subsolar point. As a result, during the OH observations the smallest SZA was 41°, which occurred early in the mission at about 0930 local solar time, and observations near the end of the mission are confined to SZAs $> 70°$ everywhere.

4. Instrument Description and Performance

4.1. Overview

The MAHRSI instrument is composed of four subsystems: the telescope/spectrograph assembly, the electronics controller assembly (MECA), the detector electronics assembly (MDEA), and the high voltage power supply (HVPS). The telescope/spectrograph assembly is an $f/7.5$, 0.75 m focal length, field-flattened Czerny-Turner spectrograph fed by a 0.5 m focal length spherical telescope with a 57 cm^2 aperture, and uses a magnetically focused intensified CCD (ICCD) detector. The wavelength range of sensitivity is from 195 to 320 nm, and the spectral resolution of the instrument at 310 nm is 0.02 nm, and at 215 nm it is 0.026 nm. A spectral bandwidth of approximately 4 nm is imaged on the focal plane at a given grating position, and the grating can be scanned to cover the entire spectral range of the instrument. A superpolished plane scan mirror at the baffled aperture of the telescope controls the vertical motion of the 0.01° by 1.13° field of view. A dust door protects the optics during launch and landing, but was open at all times on-orbit. A rotating polarizing filter was included to measure the polarization of the observed radiance.

On-orbit, MAHRSI was controlled by the microprocessor-based MECA, which managed the command and data interface to the spacecraft, controlled the dust door motor, the scan mirror motor, the polarizer wheel motor, and the grating motor, monitored the payload health indicators, and provided power distribution and control to the MDEA. The MDEA provided power distribution to the HVPS, operated the CCD

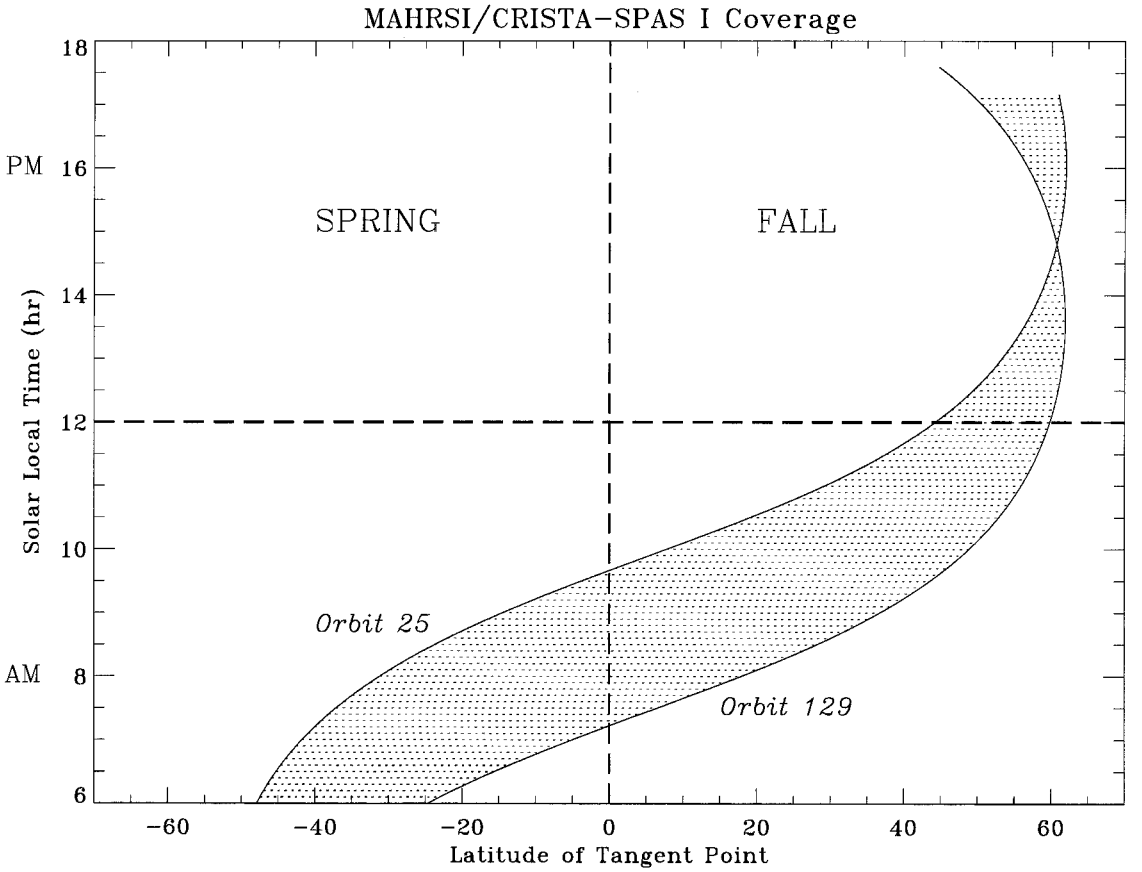

Figure 2. Distribution of MAHRSI observations with local solar time and latitude of the tangent point. Sampling of the diurnal variation is weighted toward morning hours with observation after 1200 LST confined to high northern latitudes where solar zenith angles were >60°.

detector bias and clock regulators, and after each integration, transferred serial data from the CCD to MECA. MDEA also controlled the thermoelectric coolers which kept the CCD at a temperature of approximately −28°C.

4.2. Optical Design

4.2.1. Design considerations. The primary design goals of the MAHRSI spectrograph were driven by the requirement to acquire spectra with sufficient spectral resolution to allow accurate discrimination of the OH signal from the background formed by the Rayleigh scattering of sunlight along the line of sight when observing the upper stratosphere. Plate 2 compares the positions and emission rate factors for several rotational lines in the fluorescence A–X (0, 0) band computed by *Stevens and Conway* [this issue] with a high-resolution solar spectrum [*Kurucz et al.*, 1984] in the same wavelength region (307.8–310.6 nm). This Plate makes clear the need for high spectral resolution in rejecting the bright solar Fraunhofer spectrum that lies between the discrete positions of the OH lines. Since the Doppler widths of the individual lines emitted from the mesosphere are less than 0.001 nm, the resolving power could be as large as 300,000. However, preflight model calculations indicated that a spectral resolution of 0.01 nm would be acceptable, and other considerations set the actual value. An off-axis Czerny-Turner mount with an optical speed of $f/7.5$ and a focal length of 750 mm was selected on the basis of mechanical size and mass, stray light management, throughput, and the ability to flatten the focal surface so that a passband of 4.0 nm could be focused on a two-dimensional (2-D) detector. The extended passband effectively increased the throughput of the instrument by providing the simultaneous detection of several OH features and permitted the unambiguous determination of the correct magnitude of the background spectrum. The optical scheme of *Reader* [1969], which places the grating offset from the optical centerline, was used to minimize spherical aberration, correct coma, and flatten the focal field by optimizing the placement of the grating and spectrograph mirrors. To accommodate the second objective of the experiment, which was to measure the resonance fluorescence NO γ (1, 0) band at 215 nm, the grating was mounted in a rotation mechanism pivoted to vary the offset of the grating from the optical axis and optimize placement for both grating angle settings.

4.2.2. Optical path. Figure 3 shows the mechanical layout of the instrument and the optical path. At the entrance of the 1375 mm telescope tube, 1350 mm from the spherical mirror, is a flat scanning mirror located within a baffled housing. The 145 × 85 × 15 mm superpolished Zerodur flat mirror has a surface microroughness of better than 0.1 nm rms and is coated with Al and Al_2O_3. The scan mechanism consists of a worm gear driven by a stepper motor through a reduction head resulting in line of sight motion of 2.28 arc sec per motor pulse. Attached to the worm gear is an Itek 15 bit shaft angle encoder, which provides a line of sight position resolution of 79 arc sec per encoder step. For observation from an orbital

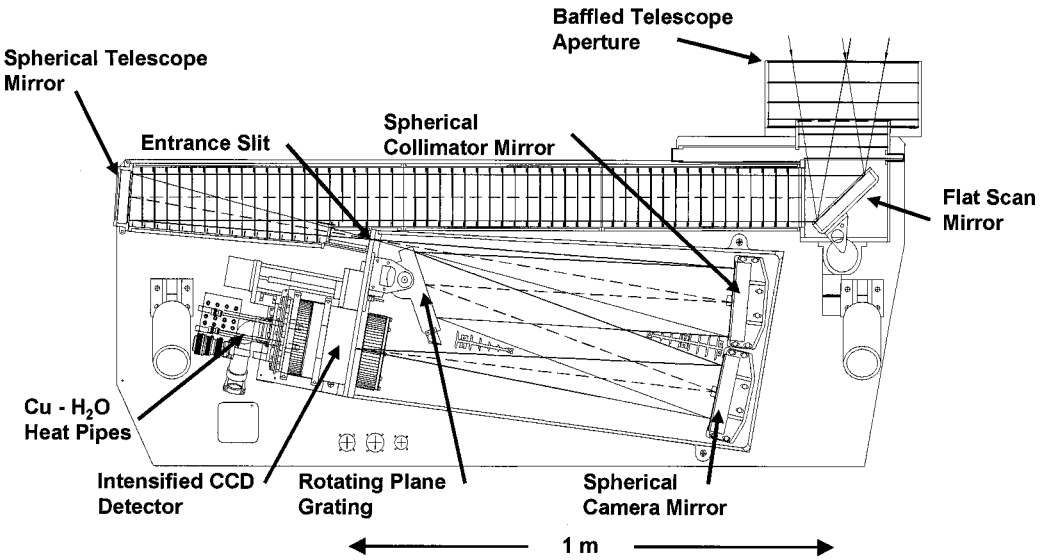

Figure 3. The mechanical and optical layout of the instrument. The optical path is described in detail in the text.

height of 300 km, this corresponds to a sampling granularity of 700 m at a tangent height of 50 km. A dust door in the scan mirror housing protected the scan mirror and telescope aperture from particle contamination during launch and landing. During integration and testing a removable cover protected the entire assembly. The telescope tube is extensively baffled. The 85.5 × 67 mm spherical telescope mirror and the spectrograph mirrors were manufactured by Muffoletto Optical with a surface roughness of less than 1.2 nm rms and were coated with Al and MgF_2. The telescope mirror is used off-axis and is positioned to place its tangential focus on the entrance slit.

A polarizing filter manufactured by overcoating a 3 mm thick fused silica disk with Polacoat is located between the telescope mirror and the entrance slit. This filter is mounted in a ring gear mechanism that allows 360° rotation in a plane perpendicular to the optical path. A 60° sector of the filter disk was removed to provide a filter position with an unobstructed optical path. The adjacent sector was overcoated with Al on the surface toward the telescope mirror to provide a position that reflected all incoming light back out through the telescope. Precise measurements of the detector dark field were obtained by periodically placing the filter in this "closed" position during orbital night. The goal of this filter was to provide an additional tool to minimize the apparent intensity of the Rayleigh scattering, which is highly polarized for scattering angles near 90°. However, the spectrograph itself was measured to have a polarization, $(P_\perp - P_\parallel)/(P_\perp + P_\parallel)$, of 75% at 308 nm, so that placement of the filter in a polarizing position would drastically reduce the throughput of the instrument even to unpolarized light (including the OH resonance fluorescence emission). As a result, virtually all observations were conducted with the filter in the "open" position.

The spectrograph entrance slit was manufactured by an electro-form process. A Grant microdensitometer was used to measure the mean width at 54.18 μm with a standard deviation of 0.16 μm; its height is 10 mm. Both the collimator and camera mirrors measure 135 × 108 mm, but the collimator mirror is masked to the projected size of the grating. The holographically ruled plane grating measures 154 mm × 88 mm and has a ruling density of 4960 grooves/mm. The entire spectrograph and the ICCD camera assembly are mounted on an optical bench built from a single 12.7 mm thick titanium plate. A titanium aperture plate rigidly attached to the optical bench supports the slit holder and grating drive, and contains an aperture for the cylindrical camera. The grating rotation mechanism also includes an Itek 15-bit shaft encoder to permit precise positioning of the grating with a resolution of 0.011°/encoder step. The spectrograph was operated in first order, and the angle of incidence at the grating is −42.5° for 308 nm and −24.6° for 215 nm giving a projected grating size of 113 × 108 mm and 140 × 108 nm, respectively. The angle between the incident and dispersed rays was 16°. The optical bench was kinematically mounted to a pocketed aluminum mounting plate 76 mm thick. This arrangement worked well to control image motion and preserve focus for the operating temperature excursions experienced on orbit (22°C to 12°C). Although no defocusing was observed, the image moved about 0.1 mm in the dispersion plane as the spacecraft emerged from the cold orbit night and gradually warmed during the day.

4.2.3. Scattered light. Great care was taken to control scattered light in the instrument. An optical ray tracing program was used to compute the exact size and placement of an extensive system of baffles. In addition to the telescope aperture and tube, particular care was taken to assure that for all grating angles, no direct light paths were available between the collimator mirror and the 10.8 × 32.4 mm active region of the detector. The interior walls of the spectrograph were well baffled, and a zero-order trap was located along the wall nearest the telescope. Extensive preflight testing with white light identified mechanical modifications which removed the most important scattering sources.

4.3. Intensified CCD Detector and Electronics

4.3.1. Detector. The MAHRSI intensified CCD (ICCD) detector consists of an EG&G Reticon RA1200JAF-021 full frame CCD fed by an ITT F-4152 single stage magnetically focused image intensifier. The CCD is an array of 400 × 1200 27 micron square pixels with a usable spectral response from

450 to 1050 nm. It was provided by the manufacturer encapsulated with a fiber-optic window. The three-phase buried channel CCD was operated in the "multipinned phase" mode to minimize dark current generation in the interface surface states. The CCD was cooled during flight to approximately −28°C to provide low dark current, low noise, and high dynamic range performance.

The image intensifier tube has a semitransparent cesium telluride photocathode deposited on a 6 mm thick fused silica window and provides 40 mm of active area. A 17.75 kV potential accelerated photoelectrons produced in the photocathode toward a standard P-20 phosphor screen that was held at ground potential. An Al shield adjacent to the screen is opaque to incoming photons incident on the intensifier but is transparent to the energetic electrons. The fiber-optic output window of the intensifier was joined to the CCD window with a thin layer of optical room temperature vulcanizing compound (RTV). A cylindrical magnet produced highly uniform field lines along the axis of the intensifier tube to minimize the width of the detector point-spread function. The maximum field strength along the central axis of the tube was approximately 250 Gauss. The field lines serve to constrain photoelectron paths as they traverse the tube and impinge on the phosphor. Since the photoelectrons spiral around the field lines as they are accelerated by the 17.75 kV electric potential, it is necessary to match the magnetic and electric fields to produce an integral number of spirals. The required relationship between field strengths is given by $V = 8.91 \times 10^9 \times (LB/n)^2$ volts, where L is the photocathode to phosphor screen distance (meters), B is the magnetic field strength (tesla), and n is the number of spirals. Laboratory measurements of platinum and iron lamp emission spectra indicated that MAHRSI's resolution was highest, with a full width at half maximum (FWHM) of 0.02 nm, when an electric field of 17.75 kV was applied across the intensifier tube.

4.3.2. Readout electronics and telemetry format. Programmable digital-to-analog converters (DACs) in the MDEA independently controlled all MAHRSI CCD bias levels and clocks and allowed flexibility in image content and readout. Clocking waveform sequences stored as microcode in programmable read-only memory (MDEA PROMS) controlled the output of the DACs. The microcode sequences directly accomplished charge shifting, summing, and readout, and the appropriate sequence was selected using uplinked commands sent to MDEA by MECA. Charge packets shifted out of the CCD were presented to the input of a 16-bit analog-to-digital (A/D) converter, and the converted 1024 pixels were recorded to the ASTRO-SPAS tape recorder as 16-bit digital numbers (dn) ranging in value from 0 to 65,535.

In order to reduce telemetry requirements of the instrument, 305 rows were summed together into the CCD's horizontal readout shift register, and pixels containing the column sums were read out at a 25 kpixel s^{-1} rate and incorporated into the telemetry stream. Overall system bandwidth allowed 1024 pixels of summed image data along with all associated instrument housekeeping data to be read out every 2.226 s. The instrument has no shutter. At the end of every integration the content of the CCD was collapsed with a "vertical" sum procedure that was completed in 49 ms. The next integration proceeded as the readout of the 1024 pixels was performed. A consequence of the operating mode was that the individual pixels always contained charge quantities far below full-well so that image degradation by blooming was never observed.

4.4. Dark Field, Temporal Noise, and Flat Field Response

The first step in determining the radiance of OH emissions and background scattering was to remove signal-independent fixed pattern and dark field contributions from the raw 305-row sums. For a single 2.226 s exposure the net signal-dependent response of the ICCD, $S(\bar{x})$, is given by

$$S(\bar{x}) = \frac{S^t(\bar{x}) - S^d(\bar{x}, T)}{U(\bar{x})} \text{ (dn)} \tag{2}$$

where

$\bar{x}$ pixel position in the 305-row sum;
$S^t(\bar{x})$ total raw pixel value (16 bits per pixel) measured at position $\bar{x}$;
$S^d(\bar{x}, T)$ dark field at temperature T;
$U(\bar{x})$ normalized spatial responsivity nonuniformity.

Extensive laboratory measurements were made preflight to characterize the signal-independent fixed-pattern dark field, temporal dark noise, and flat-field response of the MAHRSI CCD over the temperature range from −30°C to 0°C.

Since the total number of thermally generated electrons per pixel is highly sensitive to CCD temperature, and since thermistors mounted on the thermoelectric coolers are only accurate to about 1 K, it was necessary to make frequent measurements of the dark field on orbit. The most practical way to make the measurement in a shutterless instrument was to mask a small region of the CCD with black paint that is opaque to green photons from the phosphor. The horizontal shift register and first several columns of the MAHRSI CCD were painted for this purpose. These opaque columns are used to scale laboratory and on-orbit dark-field measurements. At an operating temperature of −28°C the 305-row sum dark field was measured to be 850 dn s^{-1} $pixel^{-1}$, which corresponds to approximately 5610 dark electrons s^{-1} $pixel^{-1}$ in the sum, or 19 dark electrons s^{-1} $pixel^{-1}$ in the 2-D image. The full-well capacity for an image pixel is 337,000 electrons and about 463,000 electrons/pixel for the horizontal shift register. The signal-independent noise, which includes electron shot noise in the CCD and readout noise in the electronics, was measured to be approximately 78 electrons s^{-1} $pixel^{-1}$ for the 305-row sum.

The CCD gain conversion constant at −28°C, 6.6 electrons dn^{-1}, was determined by measuring the temporal variance in dn of the CCD output as a function of the mean dn of the CCD output over a range of incident intensities and integration times. These measurements were made without the image intensifier. The measured variance of the output, if specified in electron units, is equal to the mean value of the output measured in electron units for a shot noise process, so the relationship between dn and number of electrons can be determined.

In conjunction with these measurements the gain of the preamplifier between the CCD and A/D converter was set to provide linear response over the full dynamic range of the A/D output. On-orbit measurements indicated that the observed airglow radiances were well within this range: the maximum signal observed during the mission (after dark-field subtraction) was about 50,000 dn, and the minimum signal was near 0 dn.

The nonuniformity of the ICCD responsivity was measured by illuminating the detector with a spatially flat intensity distribution. Differences in the responsivity of each pixel, the quantum efficiency of the photocathode in different locations,

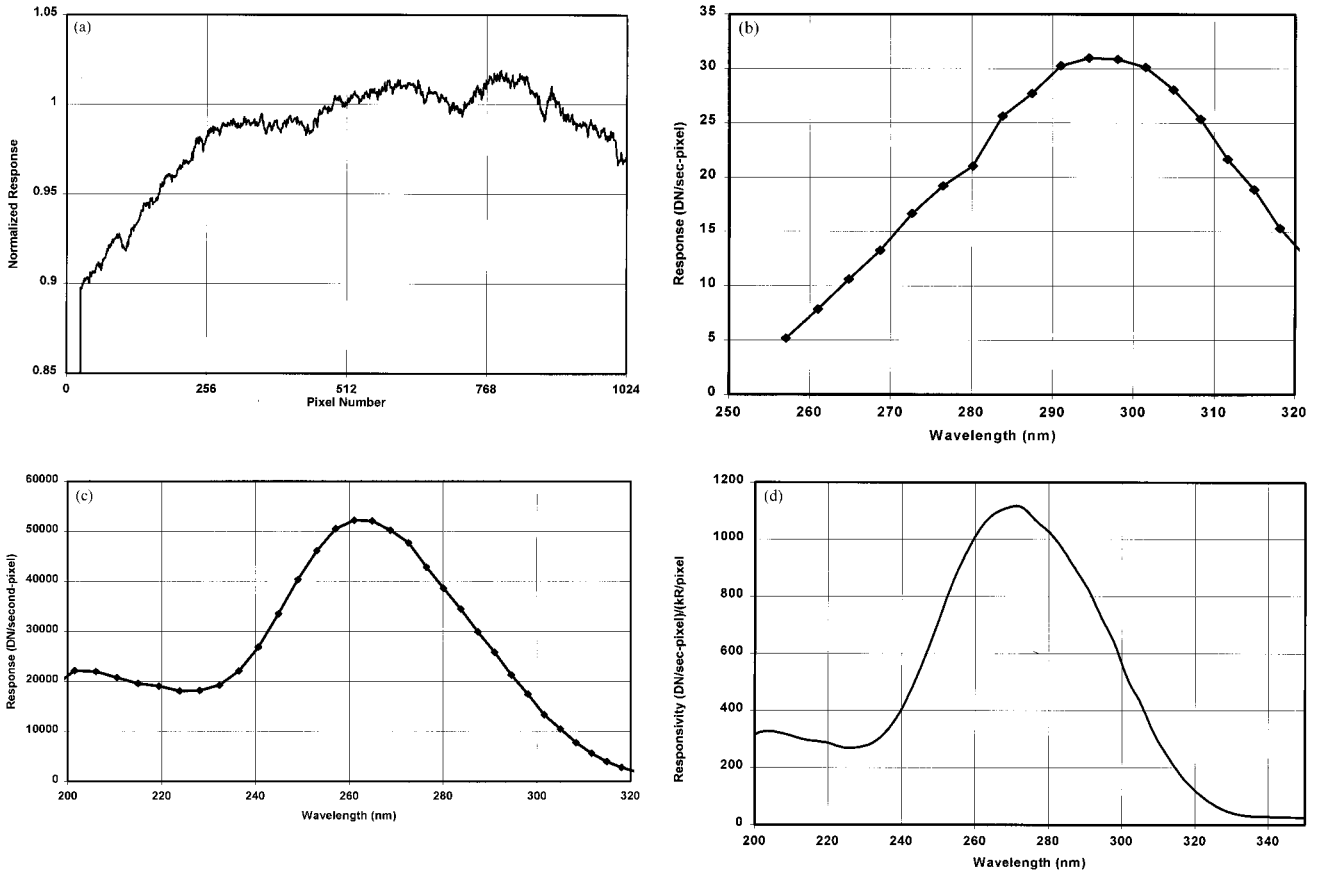

Figure 4. (a) Nonuniformity of the responsivity of the ICCD detector. (b) Response of the instrument to the radiance from an integrating sphere fed by quartz-halogen lamps. (c) Response of the instrument to the radiance from a D_2 lamp. This spectral shape was normalized to the absolute response to the quartz-halogen radiance source to estimate the response over the entire wavelength range shown in Figure 4d. (d) Final responsivity of the instrument. At 308 nm, 1 photoevent produces 11.0 dn.

and the radiant power gain of the phosphor in different locations, resulted in variations in the digitized output of the CCD. The ICCD was operated in a vacuum chamber at a temperature of −28°C. An integrating sphere fed by a Hg pen lamp was used to illuminate the photocathode, and a baffle was used between the sphere aperture and the photocathode to ensure flat field irradiance. The response of the detector to this irradiance, shown in Figure 4a, exhibited a 3% standard deviation about its mean value, and a maximum deviation of about 10%. These fall well within the 10% manufacturer nonuniformity specification for the image intensifier tube and the 5–10% manufacturer nonuniformity specification for the CCD. Measurements demonstrated that the nonuniformity result was temperature-independent between −30°C and 0°C.

4.5. Spectral Responsivity

4.5.1. ICCD. The spectral responsivity of the ICCD alone was measured using the flat-field procedure discussed above. The irradiance at the location of the photocathode was measured using a photodiode with a quantum efficiency of 19.4% at 253.7 nm (calibrated at the National Institute for Standards and Technology (NIST)) with the CCD operated at −28°C. Multiple measurements were made so that any errors in the derived responsivity due to errors in the measurement of the distance from the sphere to the photodiode or ICCD could be reduced and quantified.

The responsivity determined from these measurements is 1.29 dn photon^{-1} at 253.7 nm, with a standard deviation of 0.039, or about 3%. The responsivity of the ICCD at all other wavelengths was determined using photocathode quantum efficiency measurements provided by the manufacturer. It should be noted that the 3% uncertainty at 253.7 nm, and any uncertainties in the manufacturer measurements do not affect the final MAHRSI instrument responsivity results, since those results were derived directly using the full instrument with ICCD fed by telescope and spectrograph optics. The ICCD responsivity was primarily used to derive the gain conversion factor for the ICCD, which had a value of 11.0 dn photoevent^{-1} for the OH channel and 12.6 dn photoevent^{-1} for the NO channel. This factor, which was determined by dividing the ICCD responsivity by the quantum efficiency of the photocathode, was used to estimate the photon shot noise associated with atmospheric limb measurements.

4.5.2. Spectrograph and ICCD. The responsivity of the full MAHRSI instrument was measured by completely filling the field of view with the radiance from a large 51 cm diameter integrating sphere with a 16.84 cm clearance hexagonal output aperture. The sphere was fed by two 45 watt and two 150 watt quartz halogen lamps and contains a combination of pentagon- and hexagon-shaped Spectralon tiles. A photopic map of the sphere output performed at Labsphere, Inc. shows that the

Table 1. Overall Calibration Accuracy ε at 308 nm

Uncertainty Contributions	$+\varepsilon$, %	$-\varepsilon$, %
Precision of MAHRSI integrating sphere response measurement	0.3	−0.3
Accuracy of SSBUV integrating sphere radiance measurement	1.5	−1.5
Precision of MAHRSI D_2 lamp response measurement	<0.1	<0.1
Accuracy of NIST D_2 lamp spectral shape	<0.1	<0.1
Estimated change in responsivity between preflight and postflight calibration	N/A	−5.4
Estimated calibration accuracy at 308 nm	+1.8	−7.2

N/A, not applicable.

radiance is uniform to about ±0.2% in the central part of the sphere aperture visible to the MAHRSI instrument during calibration.

The absolute spectral radiance of the sphere was measured at the NASA Goddard Space Flight Center Laboratory for Atmospheres in collaboration with the SSBUV group [*Hilsenrath et al*., 1993; *Janz et al*., 1996]. The calibration was derived by comparing the radiance with another $BaSO_4$-coated integrating sphere's radiance which had been previously calibrated using a NIST-calibrated type FEL lamp. The error in the measurement is estimated to be 1.5% at a wavelength of 260 nm and 1.53% at 350 nm.

The integrating sphere does not produce sufficient radiance at wavelengths shortward of 260 nm to be useful for calibration. In order to extend the MAHRSI calibration to 200 nm the collimated beam from a bright deuterium lamp was reflected from a large Al-MgF_2-coated spherical concave mirror into the MAHRSI aperture. The mirror was positioned so that the D_2 lamp irradiance was out of focus at the aperture, thereby completely filling the instrument optics. The absolute radiance of the D_2 lamp/collimating mirror combination is not known to the same accuracy as the integrating sphere radiance, but the spectral shape of the lamp's emission and the mirror reflectivity are well known. The resulting responsivity spectral shape measured using the D_2 lamp can be normalized to match that measured using the integrating sphere in the wavelength range 280 to 320 nm.

The instrument response to the integrating sphere irradiance is shown in Figure 4b. The estimated measurement precision is 0.3% at all wavelengths in the range 280–320 nm. The response of the instrument to the D_2 lamp, shown in Figure 4c, was measured over the full wavelength range from 200 to 320 nm. The estimated precision of this measurement at each wavelength is better than 0.1%. Figure 4d shows the room temperature responsivity derived by dividing the response curves by the intensity curves for each of the two sources, and then normalizing the D_2 result to match the integrating sphere in the longer wavelength region. The normalized D_2 curve is used to specify the overall instrument responsivity, which converts dn to radiance units. The final conversion from dn to kR was determined from the values shown in Figure 4d by multiplying by 2.226 s (exposure time) and by 305 (number of summed CCD rows). In addition, the responsivity at each wavelength was increased by 4% to account for the laboratory-measured increase in responsivity at −28°C (the on-orbit operating temperature) relative to the responsivity at room temperature. The conversion at 310 nm wavelength is 52.6 dn s^{-1} $pixel^{-1}$ $(kR/0.01\ nm)^{-1}$, where 1 photoevent (or count) produces 11.0 dn, and that at 215 nm is 73.8 dn s^{-1} $pixel^{-1}$ $(kR/0.01\ nm)^{-1}$ where 1 photoevent produces 12.6 dn.

In addition to the estimated responsivity errors discussed above, there is a significant uncertainty due to drift of the integrating sphere intensity over time. The estimated total accuracy of the responsivity curve at 308 nm is (+1.8%, −7.2%). The overall responsivity accuracy estimates at 308 and 215 nm are summarized in Tables 1 and 2.

4.6. Wavelength Calibration

An accurate wavelength scale for the entire 195 to 320 nm spectral range of the instrument was determined preflight in the laboratory using emissions from iron and platinum hollow-cathode lamps. These measurements were used to determine the dispersion over the full spectral range for the derivation of instrument responsivity. However, the most accurate wavelength scale for reduction of the OH data was derived from the on-orbit measurements of the OH fluorescence and Rayleigh-scattered sunlight spectra.

4.7. Spectral Resolution

A critical requirement of the MAHRSI instrument is that the spectral resolution be sufficient to exactly register a reference Rayleigh-scattered solar spectrum to the spectra observed at each altitude for background subtraction. A resolution of 0.02 nm FWHM at 308 nm was achieved using a high ruling density grating, a long focal length, high precision optics, a magnetically focused image intensifier tube, and a fiber optic intensifier-CCD coupling. The upper panel of Figure 5 shows the image of a single line in the OH emission spectral region measured in the laboratory using a platinum hollow-cathode lamp. A Czerny-Turner spectrograph produces curved spectral line images at the focal plane, and this curvature is apparent in the image. The curvature, which changes slightly across the focal plane, is small in the OH emission region (307.8–310.6 nm) and is even less evident in the NO emission region (214–216 nm). As discussed earlier, the low data transmission rate available during the mission necessitates summing 305 CCD rows together before transmission to the tape recorder. Thus the summing of curved spectral lines produces a slightly asymmetric distortion of the instrument spectral resolution function as is shown in the lower panel of Figure 5. The plate factor in the OH region is 0.0039 nm/pixel so the full width half maximum of the image is slightly less than 0.02 nm. Accurate comparison of theoretical spectra to the MAHRSI limb mea-

Table 2. Overall Calibration Accuracy ε at 215 nm

Uncertainty Contributions	$+\varepsilon$, %	$-\varepsilon$, %
Precision of MAHRSI integrating sphere response measurement	0.3	−0.3
Accuracy of SSBUV integrating sphere radiance measurement	1.5	−1.5
Precision of MAHRSI D_2 lamp response measurement	<0.1	<0.1
Accuracy of NIST D_2 lamp spectral shape	0.8	0.8
Estimated change in responsivity between preflight and postflight calibration	N/A	−11.6
Estimated calibration accuracy at 215 nm	+2.6	−14.2

surements and the use of ground-based solar spectra to estimate the shape of the Rayleigh-scattering spectrum required the spectral resolution function to be measured with high precision at all locations on the focal plane. The plate factor in the NO region is 0.0058 nm/pixel, and the full width half maximum of the spectral resolution function for NO observations is 0.03 nm.

4.8. Polarization

A polarizer wheel was developed to insert a linear polarizing element into the optical path to reduce the Rayleigh-scattered sunlight component of the signal relative to the unpolarized fluorescence (the polarization of the fluorescence radiation is less than 5% (D. Crosley, personal communications, 1996). However little use was made of the filter because it substantially reduced the instrument throughput. Although the polarization of the MAHRSI instrument was measured before flight at each position of the wheel, we report here only the method and the results for the "open" position.

As stated in section 4.2, the other optical elements of the instrument, especially the grating, combine to make the spectrometer a polarized device. The MAHRSI polarization was measured following the method described by *Kudo et al.* [1969]. The measurement was carried out at 313.0 nm using a Hg Pen-Ray lamp as a source. A lamp holder with a 3.5 mm diameter aperture was placed at the focus of a quartz lens to produce a collimated beam. Two auxiliary rotatable polarizer filters (a PL-40 and a PL-37), a Pyrex (Corning 7740) cutoff filter, and a 10.8 mm circular aperture completed the setup. These items were assembled on an optical bar and aligned to the MAHRSI optical axis. A solar blind (CsTe photocathode) photon counting detector was installed in the focal plane and scanned to the peak of the Hg 313.0 nm line. By observing the peaks and minima of the count rate the parallel and perpendicular positions were found for each external polarizer. The maximum transmission occurs when the E vector is horizontal (perpendicular to the rulings on the grating). Using this technique, a value of P_M for each setting of the polarizer wheel was measured. The results for the open position were 75% with a measurement precision of ~5% or better, confirming that MAHRSI is a highly polarized instrument.

4.9. Field-of-View Function and Off-Axis Light

The field-of-view function of the instrument was measured in the laboratory by illuminating the aperture of the telescope using the expanded and collimated beam of 320 nm radiation from an HeCd laser. The results imply that the response of the instrument on orbit is lower by 10^{-4} at an angle of 0.02° from the center of the line of sight in the direction toward the bright limb, and by 10^{-5} at an angle of 0.13°. Convolution of the function with a model Rayleigh-scattering intensity profile predicts that when viewing the limb at a tangent height of 70 km, only 1.6% of the signal is due to light outside of the nominal field of view. The laboratory measurement of the field of view does not completely account for light that may be scattered into and dispersed by the instrument from large angles off-axis by the mechanical structure of the telescope aperture light baffle. The lack of a quantitative measure of this signal does not impact the retrieval of OH radiance profiles because it is included in the background subtraction, but it does represent a source of error in the measurement of the Rayleigh-scattering radiance.

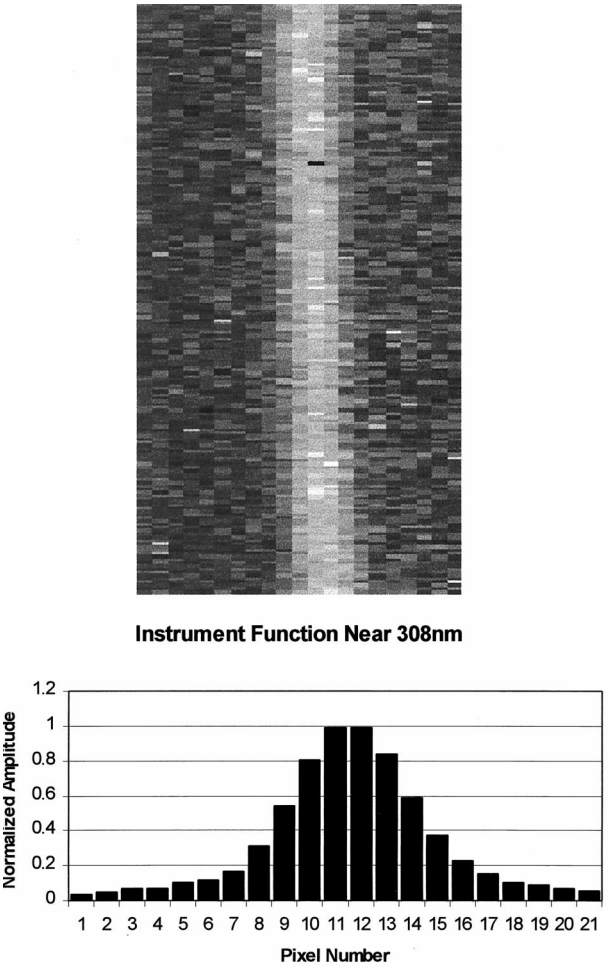

Figure 5. Image of a single emission line from a platinum hollow-cathode lamp is shown in the upper panel. Each pixel is 27 microns wide. The vertical sum of 305 rows produces the line shape shown in the lower panel.

4.10. Data Reduction

Data reduction and calibration entails removing instrumental effects, registering the wavelength scale with a reference Rayleigh-scattering spectrum, removing noise and energetic particle spikes from spectra using a statistical discrimination technique, scaling and subtracting Rayleigh-scattered solar background, measuring and accounting for ozone absorption, integrating over spectral regions of interest, and converting the digitized output of the CCD to radiance units with error estimates. The resulting radiance profiles are then inverted to derive number density profiles.

As discussed earlier, the raw digital numbers downloaded in the telemetry, $S'(\bar{x})$, are corrected for ICCD dark field and responsivity nonuniformity to derive signal-dependent digital numbers, $S(\bar{x})$. These digital numbers are then associated with wavelength and converted to kR units,

$$4\pi I(\lambda) = \left[\frac{S(\lambda)}{\Delta\tau_{\text{int}} R(\lambda)}\right] (\text{kR}/0.01\ \text{nm}) \tag{3}$$

where $\Delta\tau_{\text{int}}$ is the integration time in seconds and $R(\lambda)$ is the instrument responsivity in dn s^{-1} pixel^{-1} (kR/0.01 nm)$^{-1}$.

4.10.1. Thermal response of the spectrograph. Although the spectrograph optical bench and grating mounting plate

were fabricated from titanium in order to minimize movement of critical optical elements due to anticipated temperature variations during flight, small temperature-dependent shifts in the location of the spectrum on the image plane were observed. Typically, the image gradually shifted by as much as 4 pixels (about 100 microns) during a single orbit as the instrument passed from orbit night into full Sun. This corresponds to a wavelength shift of approximately 0.016 nm and could lead to significant errors when a reference background spectrum is subtracted. An autocorrelation technique was used to correct this apparent wavelength shift problem. Owing to the highly structured nature of the solar spectrum, the technique was so sensitive that it was able to measure the thermal shift to within approximately 0.05 pixel. A cubic spline interpolation was used to estimate the intensity that would be observed by CCD pixels if the imaged spectrum were shifted slightly with respect to the focal plane. As discussed in the error section below, inaccuracies introduced by the interpolation procedure result in less than 1.5% errors in the final subtracted OH spectrum.

Spectral images also exhibit fairly large noise spikes, probably due to cosmic rays or energetic particles incident on the detector, that do not fall within the expected 3σ temporal noise estimate. A statistical discrimination technique is used to remove the spikes both inside and outside OH emission spectral regions prior to solar background subtraction.

4.10.2. Retrieval of OH radiance profiles. In order to determine the OH radiance present in a limb measurement at a tangent height z, $I_{\text{limb}}(\lambda, z)$, a nonlinear least squares curve fit is used to determine the constants C_1–C_4 in the following equation:

$$I_{\text{limb}}(\lambda, z) = (C_1(z)B_0(\lambda) + C_2(z)\tilde{I}_{\text{OH}}(\lambda, T(z)) + C_3(z)) \cdot \exp(-C_4(z)\sigma_{\text{O3}}(\lambda, T(z)) - \tau_{\text{R}}(\lambda)) \quad (4)$$

where

$B_0(\lambda)$ is a reference background spectrum free of OH emission or absorption;
$\tilde{I}_{\text{OH}}(\lambda)$ is the theoretical OH emission spectrum;
$\sigma_{\text{O3}}(\lambda, T(z))$ is the ozone cross section at temperature $T(z)$ [*Bass and Paur*, 1985];
$\tau_{\text{R}}(\lambda)$ is the Rayleigh scattering optical depth along the viewing path.

The constant term $C_3(z)$ accounts for slight inaccuracies in the dark-field subtraction and also serves as a proxy for the filling in of the Fraunhofer absorption features resulting from the Raman scattering of sunlight by N_2 and O_2, that is, the Ring effect [*Grainger and Ring*, 1962].

The reference background $B_0(\lambda)$ was determined by correcting the ground-based observation of the solar irradiance reported by *Kurucz et al*. [1984] for extinction by OH and ozone, normalizing to an exoatmospheric spectrum, and convolving with laboratory-measured MAHRSI spectral resolution functions. *Stevens and Conway* [this issue] discuss this procedure, as well as the procedure for calculating the OH emission spectrum $\tilde{I}_{\text{OH}}(\lambda)$ in detail. The use of the ground-based spectrum is a potential source of systematic error in the residual spectrum because its shape may not include detailed variations of the instrument function across the focal plane. To test for the presence of such errors, OH intensities were also retrieved using a reference spectrum composed of observations of the moon made by MAHRSI during the flight. It was found that the OH intensities retrieved using this background were 1% less at 70 km and 11% less at 50 km. Much of the error at the lowest altitudes was attributable to the lower signal-to-noise ratio of the lunar spectrum, so ultimately the ground-based-derived background was selected.

The ozone absorption cross section data of *Bass and Paur* [1985] used in the regression were measured at a spectral resolution 0.05 nm and are therefore of lower resolution than MAHRSI's 0.02 nm by more than a factor of 2. Features in the cross section resolved by MAHRSI but not by the laboratory measurements will produce spurious features in the residual spectra and may account in part for the observed standard deviation of the OH spectra.

It is important to note that the only wavelength-dependent functions used in the curve-fitting process were the reference background, the fixed shape of the OH spectrum, and the ozone cross section. No polynomial was included which could compensate for unidentified absorbers or emitters.

The curve-fitting process established the magnitude of all non-OH components of the measured spectrum. The OH contribution was then the residual remaining after subtraction of these components. Specifically, once the constants C_1–C_4 were determined by the curve-fit algorithm, the limb radiance measurement was adjusted for inferred ozone absorption and an underlying continuum, and integrated over the wavelength region $\lambda_{\text{OH}}|_f$ for each OH spectral feature f to derive the total measured OH emission at tangent height z; that is,

$$I_{\text{OH}}(z)|_f = C_{\text{srf}}|_f \sum_{\lambda \in \Gamma(\lambda_{\text{OH}}|_f)} \left[\frac{I_{\text{limb}}(\lambda, z)}{\exp(-C_4(z)\sigma_{\text{O3}}(\lambda, T(z)) - \tau_{\text{R}})} - C_1(z)B_0(\lambda) - C_3(z) \right] \text{(kR)}, \quad (5)$$

where $\Gamma(\lambda_{\text{OH}}|_f)$ corresponds to the 11 pixel region on the focal plane centered on the OH spectral feature f. The 11-pixel sum is multiplied by a constant, $C_{\text{srf}}|_f$, calculated using the instrument spectral resolution function that converts to total intensity in the feature. The average value of $C_{\text{srf}}|_f$ was 1.55. One of the best ways to validate the accuracy of the background subtraction is to compare the tangent height profiles of separate spectral features. Retrieved intensity profiles (45–90 km tangent height) for each of 11 bright OH emission features used in the inversion were found to be consistently similar in shape.

For altitudes below 55 km the reference background $B_0(\lambda)$ is corrected to account for extinction of the Rayleigh scattered radiation by ground state OH in the slant column viewed by the instrument. The extinction results in an underestimate of I_{OH} by a small amount that is dependent on the true OH density profile and on the apparent brightness of the background. The correction is discussed further in section 6.2.

4.11. Radiance Measurement Error Budget

The precision of individual OH radiance measurements is determined by estimating the photon shot noise of the limb measurement $I_{\text{limb}}(\lambda, z)$, the scaled precision of the background $B_0(\lambda)$, and the detector noise. In general, the root-sum-square of these errors is dominated by photon shot noise and ranges between 5 and 10% depending on the altitude of the tangent point. Also, a pseudorandom error of less than 1.5% due to the wavelength shifting of each limb spectrum is included in the overall measurement random error. The root-sum-square of these four random errors was computed for each altitude and propagated through the inversion algorithm to estimate the retrieval random error.

The systematic error in derived OH emission radiance is the overall responsivity uncertainty discussed in section 4.5 and summarized in Table 1. Section 6.4 discusses how the systematic retrieval error was estimated.

5. Data Inversion

5.1. Forward Model

Rewriting (1) for convenience, the intensity, or spectral radiance, observed by the MAHRSI instrument at a wavelength λ is given by

$$I_\lambda = \int_{\text{line of sight}} \frac{g_\lambda(s)m(s)Q(s)}{4\pi}\, e^{-\tau(s,\theta(s))}\, ds \tag{6}$$

where units and definitions are as for (1) with the following exceptions: (1) the fluorescence g factor g_λ is dependent on s through the temperature but is calculated for an unattenuated solar flux, (2) m is either [OH] or [NO] (molecules cm^{-3}) depending upon the given observation, and (3) τ is the absorption optical depth at solar zenith angle θ and includes both the extinction of the solar beam reaching the scattering volume, and the attenuation of fluorescence emission along the line of sight to the instrument. That is, $\tau = \tau_{\text{line of sight}} + \tau_{\text{Sun}}(\theta)$, where $\tau_{\text{line of sight}} = \sigma_M \int_s^\infty M(s')\, ds'$, $\tau_{\text{Sun}} = \sigma_M \int_{\text{path to Sun}} M(s')\, ds'$, and M represents an absorbing species. Three processes contribute to the optical depth: extinction due to Rayleigh scattering by N_2 and O_2, absorption by O_3 and O_2, and self-absorption by the fluorescing species. The mass spectrometer/incoherent scatter (MSIS) 90 [*Hedin*, 1991] model is used to supply temperature and O_2 and N_2 profiles for each latitude. The model ozone profile used is discussed in section 6.3.

Since the MAHRSI instrument takes intensity measurements approximately every 2 km in altitude, the atmosphere is modeled as a series of concentric shells of thickness 2 km. This model is illustrated in Figure 6a. The species density is assumed to be constant within each spherical shell. Notice that the solar zenith angle varies both between shells as well as along the line of sight. That is, $\theta_0 \neq \theta_0'$ and $\theta(s_0) \neq \theta(s_1)$. For any given observation the exact values for the solar zenith angles are used.

The contribution from each point s along the line of sight to the total intensity is calculated in the following manner. The extinction of the solar irradiance along the solar slant path is calculated using exact values for the solar zenith angles. The attenuated solar irradiance and the temperature-dependent g factor at s are used to calculate the OH or NO volume excitation rate. Finally, the line-of-sight column from s to the instrument is calculated, and the fluorescence signal is attenuated by the amount

$$\exp\left\{-\int_{S_k}^{\infty} (\sigma_{O_3}[O_3](s) + \sigma_{\text{self}}(s)m(s) + \sigma_{RS}[O_2 + N_2](s))\, ds\right\}.$$

By assuming $N + 1$ measurements have been taken at tangent altitudes $\{z_0, \cdots, z_N\}$ and discretizing the integral in (6), we obtain

$$I_\lambda(z_0) = \sum_{k=-N}^{N} \frac{g_\lambda(s_k)m(s_k)Q(s_k)}{4\pi}\, e^{-\tau(s_k,M)}\, ds_k^0 \tag{7}$$

Note that by the assumed spherical symmetry of $M(s)$, $m(s)$, and the temperature profile we have $m(s_{-k}) = m(s_k)$, $M(s_{-k}) = M(s_k)$, and $g_\lambda(s_{-k}) = g_\lambda(s_k)$. However, as noted previously, due to the differing solar zenith angles and slant paths, it is clear that $e^{-\tau(s_i,M)} \neq e^{-\tau(s_{-i},M)}$. Equation (7) can be rewritten as

$$I_\lambda(z_0) = \sum_{k=1}^{N} \frac{g_\lambda(s_k)m(s_k)Q(s_k)}{4\pi} \{e^{-\tau(s_k,M)} + e^{-\tau(s_{-k},M)}\}\, ds_k^0 + \frac{g_\lambda(s_0)m(s_0)Q(s_0)}{4\pi}\, e^{-\tau(s_0,M)}\, ds_0^0. \tag{8}$$

Similarly, at a tangent altitude z_j, the intensity will be

$$I_\lambda(z_j) = \sum_{k=j+1}^{N} \frac{g_\lambda(s_k)m(s_k)Q(s_k)}{4\pi} \{e^{-\tau(s_k,M)} + e^{-\tau(s_{-k},M)}\}\, ds_s^j + \frac{g_\lambda(s_j)m(s_j)Q(s_j)}{4\pi}\, e^{-\tau(s_j,M)}\, ds_j^j. \tag{9}$$

Terms for which $k < j$ do not appear in this expression, since the line of sight at tangent altitude z_j does not cut through these shells. The term ds_k^j represents the path length in the kth shell for the line of sight whose tangent altitude is z_j. As can be seen in Figure 6, $ds_j^j \gg ds_k^j$. Thus, in the absence of attenuation, the dominant term in (9) will come from the central shell, but as attenuation becomes significant,

$$e^{-\tau(s_j,M)}\, ds_j^j$$

will become small, and the dominant term will shift to a shell which lies nearer to the instrument. By summing over the MAHRSI passband and employing matrix notation, (9) can be represented in the form

$$\mathbf{I} = \mathbf{G}(\mathbf{m}) \tag{10}$$

where $\mathbf{m}$ is the vector of species number densities. Notice that due to the self-absorption term in τ, this is not a linear equation in $\mathbf{m}$.

5.2. Inverse Problem

Observational noise modifies (10) to read

$$\mathbf{I}^{\text{obs}} = \mathbf{G}(\mathbf{m}) + \varepsilon \tag{11}$$

where ε is a stochastic random variable. In nearly all cases the random error of the MAHRSI's measurements is dominated by photon shot noise so that ε will follow a Poisson distribution. The goal is to recover a profile $(m_0, \cdots m_N)$ from the set of noisy observed intensities $(I_0^{\text{obs}}, \cdots, I_N^{\text{obs}})$.

Self-absorption introduces a small nonlinearity in (11). The first step in solving for $\mathbf{m}$ is to linearize (11) by expanding $\mathbf{G}(\mathbf{m})$ in a Taylor series about a guess for the profile $\tilde{\mathbf{m}}$, so that,

$$\mathbf{I}^{\text{obs}} \approx \mathbf{G}(\tilde{\mathbf{m}}) + \left.\frac{\partial \mathbf{G}}{\partial \mathbf{m}}\right|_{\mathbf{m}=\tilde{\mathbf{m}}} (\mathbf{m} - \tilde{\mathbf{m}}) + \varepsilon. \tag{12}$$

Denoting $\mathbf{G}(\tilde{\mathbf{m}})$ as $\tilde{\mathbf{I}}$ and $\partial\mathbf{G}/\partial\mathbf{m}|_{\mathbf{m}=\tilde{\mathbf{m}}}$ as $\mathbf{F}$, (12) can be written as the linear set of equations

$$\mathbf{I} - \tilde{\mathbf{I}} = \mathbf{F}(\mathbf{m} - \tilde{\mathbf{m}}) + \varepsilon. \tag{13}$$

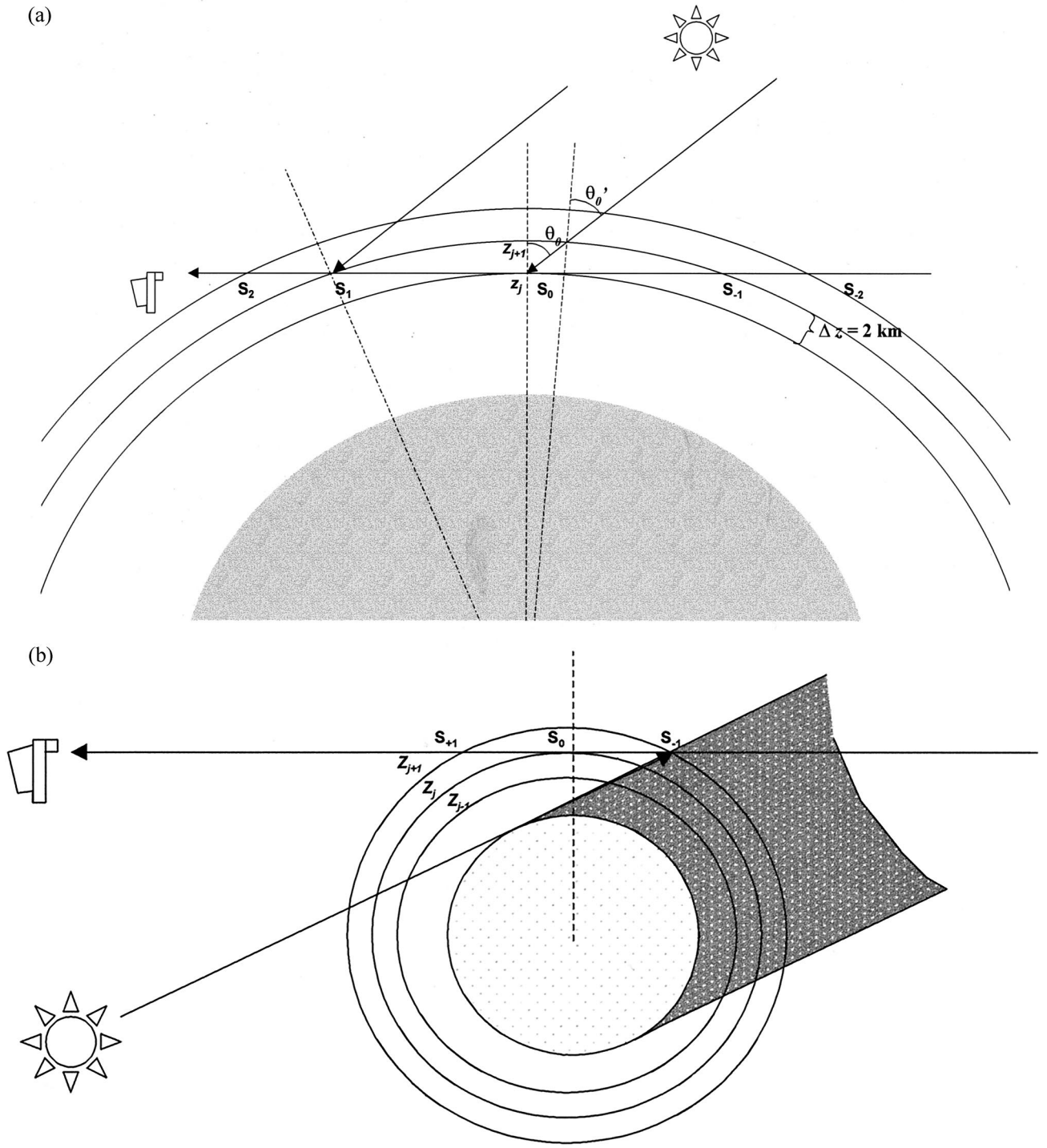

Figure 6. Geometry of the forward model for (a) nontwilight conditions and (b) twilight conditions.

Equation (13) is solved for $\mathbf{m}$, which is then used as a new $\tilde{\mathbf{m}}$ in (12) and (13). This process is repeated until $\mathbf{m} = \tilde{\mathbf{m}}$.

Equation (13) cannot be solved directly for $\mathbf{m}$ since the solution will be highly oscillatory. The reason for this is that at lower tangent altitudes, large optical depths tend to smooth out the contribution from each shell. This will cause the corresponding rows in $\mathbf{F}$ to be nearly linear combinations of one another. From linear algebra this will cause the determinant of $\mathbf{F}$ to be small. This will cause the elements of the inverse of $\mathbf{F}$ to become large, and the solution will be sensitive to small changes in the data, amplifying any noise present [*Twomey*, 1965].

A noise-filtering technique must be applied to (13) to solve for $\mathbf{m}$. Let $\| \ \|_2$ represent the so-called "L2 norm," $\|\mathbf{X}\|_2 = \sqrt{\mathbf{X}^T\mathbf{X}}$, and let η denote some upper bound on $\|\varepsilon\|_2$. Then from (13) we find

$$\|(\mathbf{I} - \tilde{\mathbf{I}}) - \mathbf{F}(\mathbf{m} - \tilde{\mathbf{m}})\|_2 \leq \eta. \tag{14}$$

Any $\mathbf{m}$ that satisfies the inequality in (14) must be admitted as a candidate profile. As there are an infinite number of profiles

that satisfy (14), a procedure must be developed which will select out the "best" solution that satisfies the inequality.

The Twomey regularization method [*Twomey*, 1963, 1965, 1975, 1977] is a systematic approach for determining the optimum **m**. This approach includes a priori information in the form of smoothness criteria that **m** must satisfy. Cast as a minimization problem, this technique says that the best profile is the solution of the following:

$$\min \|\mathbf{Lm}\|_2 \quad \text{subject to} \quad \|(\mathbf{I} - \tilde{\mathbf{I}}) - \mathbf{F}(\mathbf{m} - \tilde{\mathbf{m}})\|_2 \leq \eta. \qquad (15)$$

where $\|\mathbf{Lm}\|_2$ is a smoothness constraints which could be based on the variance,

$$\sum (m_k - m_k^{\text{a priori}})^2,$$

the sum of squares of first differences,

$$\sum (m_k - m_{k-1})^2,$$

or the sum of squares of second differences,

$$\sum (m_k - 2m_{k-1} + m_{k-2})^2.$$

Equation (15) says that from the infinite number of candidate profiles the optimum one is the smoothest one.

A standard procedure for solving minimization problems, such as (15), is to reformulate it in terms of Lagrange multipliers. When this technique is applied to (15), the result is [*Twomey*, 1963, 1965, 1975, 1977]:

$$(\mathbf{F}^T\mathbf{F} + \lambda\mathbf{L}^T\mathbf{L})(\mathbf{m} - \tilde{\mathbf{m}}) = \mathbf{F}^T(\mathbf{I} - \tilde{\mathbf{I}}) \qquad (16)$$

where λ is the value of the Lagrange multiplier. If, as we hope, λ is fairly small, then from (16) it is seen that the Twomey regularization techniques solve a set of equations which are "close to" the original set, equation (13), but which are hopefully more numerically stable. λ is a measure of the degree of smoothness that we associate with the density profile. By choosing a value of λ that is too large, the profile will be oversmoothed, possibly removing features that truly exist. If λ is too small, then the retrieved density profile is influenced by too much noise, and the profile will be highly oscillatory. Because MAHRSI is the first instrument to obtain systematic measurements of [OH] in the mesosphere, there is no profile that can be used in computing an a priori variance constraint. This problem is exacerbated by the fact that [OH] exhibits a strong diurnal dependence, so an a priori profile for the wrong solar zenith angle could skew the retrieved profile. Thus we tried both first and second differences as the smoothing constraint.

The optimum value of, λ_{opt}, was determined by employing the following procedure. A model profile corresponding to a solar zenith angle of 45° was inserted into the forward model in order to produce a synthetic radiance profile. A finer grid ($\Delta z < 2$ km) was used in the forward model in order to predict more accurately the "true" intensity. A Poisson noise component was then added onto the synthetic intensity profile. Equation (16) was solved using varying values of λ. The value of λ that yielded the best comparison with the original model density profile was taken to be λ_{opt}. At the same time, it was found that a smoothing constraint corresponding to the second derivative would yield the best results. This procedure was repeated with model profiles corresponding to solar zenith angles of 25° and 60°. In both cases the same value of λ_{opt} was obtained. This uniformity in λ for varying density profiles gave us confidence in using λ_{opt} for the observed radiance profiles.

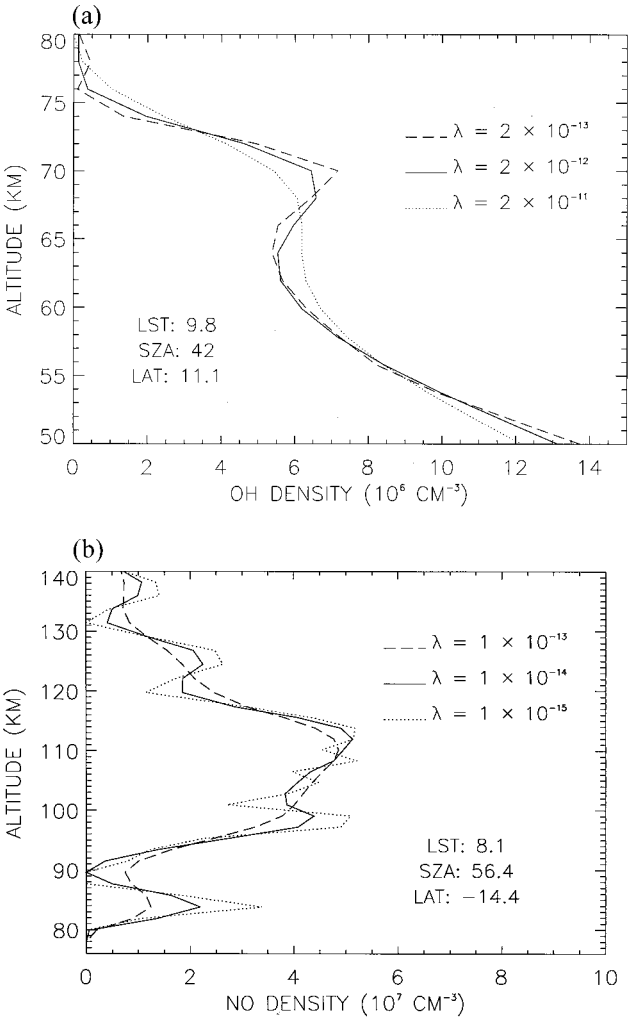

Figure 7. Results of varying the (a) OH and (b) NO inversion smoothing parameters by factors of 10 about the final value. The solid curves indicate the λ_{opt} values used for the inversion. The local solar time, solar zenith angle, and latitude for the observations are indicated.

A similar procedure was followed for the NO retrievals. Further confidence in the choice of λ for the OH retrievals was obtained by comparing the scan-to-scan variations of the retrieved profiles at 50 km, where the value of [OH] is believed to be slowly varying during most of the day, to the propagated random measurement error envelope. For the same choice of λ the variations were comparable to the random error. Figure 7 shows the results of varying the value about the value of λ_{opt}.

5.2.1. Model resolution. [OH] retrievals were computed from 90 km down to 43 km. Below 50 km the ozone optical depth becomes large enough and the emission efficiency small enough that the main contribution to the observed radiance no longer comes from the tangent point but is shifted toward the near field. This substantially broadens the retrieval averaging kernal, and little information from the tangent point is available to the retrieval. This can be seen in Figure 8 which shows the inversion "smoothing functions" for several altitudes from 70 to 45 km for a midmorning scan from orbit 27. These functions are the rows of the model resolution matrix and comprise the "averaging kernal" defined by *Rodgers* [1990].

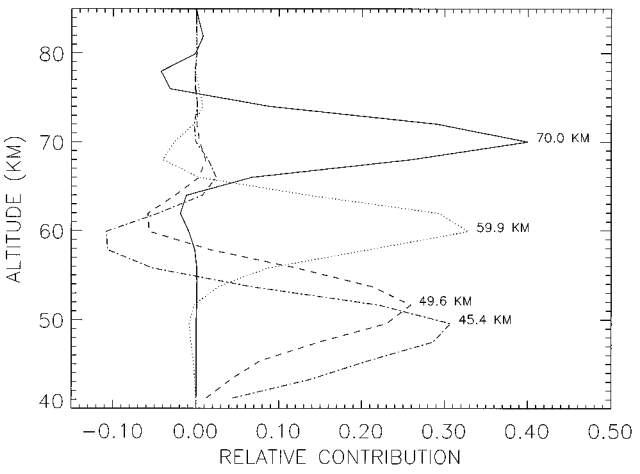

Figure 8. Rows of the model resolution matrix computed by the OH inversion algorithm for 70, 60, 50, and 45 km. These functions measure how much the inversion smoothes the "true" profile to produce the inverted profile.

5.2.2. Treatment of twilight conditions. From Figure 6a the solar beam is seen to pass through all layers with altitudes higher than z_j before reaching the volume on the line of sight in shell j. When the solar zenith angle at the tangent point is larger than about 88°, the solar beam will pass through layers for which $k \leq j$ as shown in Figure 6b. In this case the extinction must be properly calculated using model densities of O_3, O_2, and N_2 at the lower altitudes. In addition, there will be volumes along the line of sight that are not illuminated because they are in the Earth's shadow. The inversion algorithm accommodates these conditions since $\tau = \tau_{\text{line of sight}} + \tau_{\text{Sun}}(\theta)$ will yield an infinite optical depth and those terms in (9) will not contribute to the total intensity; that is, only one of the two terms from the $z_{j\text{th}}$ shell will appear in the final sum. In the case that only the higher tangent points in a limb scan are illuminated, the inverted profile only extends down to the last illuminated tangent height.

6. Results

During the November 1994 flight, MAHRSI acquired science data for nearly 189 hours. Of these, 120 hours were dedicated to OH operations and 48 hours to NO operations. The remaining time was spent on other exploratory observations, and because this was the first flight of a new instrument, a substantial amount of time was spent evaluating its performance on orbit. Before presenting a summary of the results, we first discuss in some detail the effects of collisional quenching and O_3 absorption on the OH retrievals as well as sensitivity studies for the measurement and inversion of both OH and NO. The OH data presented here are revised versions of those appearing in previous publications [*Conway et al.*, 1996; *Summers et al.*, 1996; SUM97].

6.1. Collisional Deactivation and Vibrational Energy Transfer of OH

Equation (1) can be written in more detail as follows:

$$I(\lambda, \mathbf{r}, \hat{n}) = \int \left\{ \frac{g_{00}(\lambda, \mathbf{r}')\rho(\mathbf{r}')Q_0}{4\pi} + \omega_{00}\frac{g_{10}(\lambda, \mathbf{r}')\rho(\mathbf{r}')Q_0}{4\pi\omega_{10}} \times \frac{k^{v=1\to v=0}[M(\mathbf{r}')]}{k^{\text{rad}}_{v=1} + k^{v=1\to v=0}[M(\mathbf{r}')] + k^{Q}_{v=1}[M(\mathbf{r}')]} \right\} e^{-\tau(\lambda)}\, ds$$

$$= \int \{\varepsilon_0 + \varepsilon_{v0}\} e^{-\tau(\lambda)}\, ds, \tag{17}$$

where

$$Q_0 = \frac{k^{\text{rad}}_{v=0}}{k^{\text{rad}}_{v=0} + k^{Q}_{v=0}[M(\mathbf{r}')]}.$$

Here the expression for the emission efficiency, Q, has been expanded to show explicitly the effect of collisional deactivation of the $A^2\Sigma$ state. The parameter $g_{v'v}$ is the fluorescence g factor for the (v', v'') band, $\omega_{v'v}$ is the branching ratio for the (v', v'') band, $k^{v=1\to v=0}$ and k^{Q}_{v} are the vibrational energy transfer (VET) and electronic state quenching rate constant (cm^3 molecule^{-1} s^{-1}), and k^{rad}_{v} is the radiative lifetime (s^{-1}) for level v [*Stimpfle and Anderson*, 1988]. Although $\omega_{00} = 1$, it is included in (17) for completeness. The quantity in braces is the total volume emissivity ε for the (0, 0) band. It is the sum of two terms, the first (ε_0) being the volume emissivity due to the direct solar excitation of the $v' = 0$ level, and the second (ε_{v0}) is due to excitation of the $v' = 1$ level followed by collision-induced transfer to the $v' = 0$ level. Q_0 is the emission efficiency contribution due to quenching of the $v' = 0$ level. The laboratory rate measurements of *Copeland et al.* [1985] and *Williams and Crosley* [1996] were used to estimate Q. Figure 9a shows that Q_0 is about 95% at 70 km and smoothly decreases to about 50% at 50 km. Q_0 is explicitly included in the inversion algorithm. The right-hand panel of Figure 9 shows the quantity $\varepsilon_1/(\varepsilon_0 + \varepsilon_{v0})$, that is, the fraction of the total (0, 0) emission rate due to VET for a SZA of 45°. For these conditions, 11% of the total emission from 50 km is due to VET from $v' = 1$. However, the effect of VET on the MAHRSI observation is less than Figure 9 would suggest be-

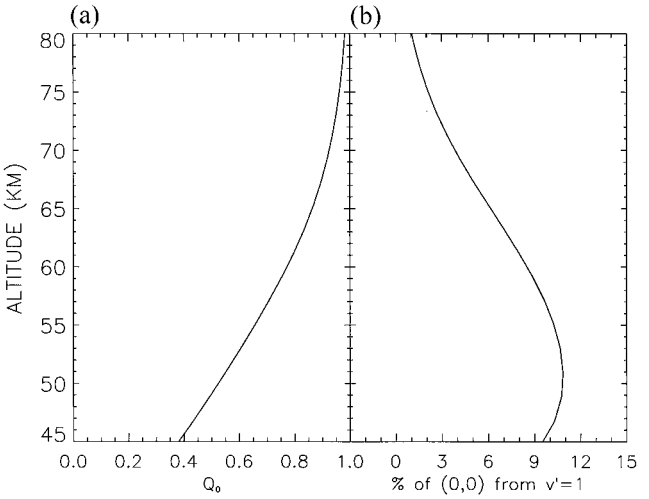

Figure 9. Effects of collisional deactivation and vibrational energy transfer of the OH $A^2\Sigma$ state on the (0, 0) band fluorescence at each altitude. (a) Altitude profile for Q_0, the emission efficiency of the $v' = 0$ level due to quenching. (b) Fraction of the total excitation of the $v' = 0$ level due to vibrational transfer from the $v' = 1$ level for a SZA of 45°. The effect of the vibrational transfer on retrieval of the OH densities is estimated to be less than 4% (see text).

cause most of the (0, 0) band emission from molecules excited by this process is in rotational lines with higher N values than observed by the instrument. Williams and Crosley report that for collisions with both N_2 and O_2, the OH rotational distribution of the $v' = 0$ molecules was nonthermal and populated higher levels than characteristic of the 300 K ambient gas temperature during their experiment. For N_2, that distribution was represented by two populations, one at 400 K, which peaked at $N = 2$, and one at 1000 K, which peaked at $N = 4$. The authors suggested that the lower temperature population may be the result of collisions subsequent to the VET and thus may not reflect the nascent population. For O_2 a similar result was found, but the higher temperature population peaked at $N = 9$. As presented by *Stevens and Conway* [this issue], 73% of the emission in the 10 brightest lines observed by MAHRSI arise from levels with $N' \leq 2$. From the populations presented by Williams and Crosley we estimate about a third of the combined population they observed for N_2 would emit from these levels. Therefore we conclude that the VET contribution to the emission observed by MAHRSI is less than 4% and probably even smaller. The effect is treated as a systematic uncertainty and not included in the inversion.

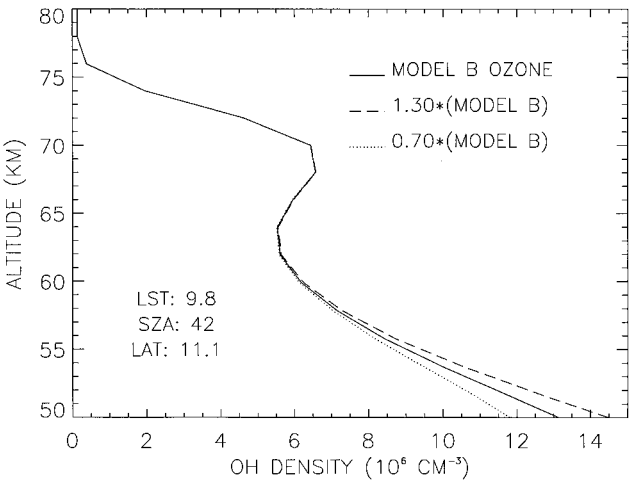

Figure 10. Sensitivity of the OH inversion to the O_3 profile used for the inversion. Version 2 uses the SUM97 Model B profile to compute the solid line profile. Scaling the O_3 profile by ±30% results in a ±10% variation in the retrieved OH density at 50 km.

6.2. OH Retrieval Sensitivity to OH Extinction of the Background Spectrum

As discussed in section 4.10, OH radiance profiles are retrieved from the data using a background, $B_0(\lambda)$, derived from a ground-based solar spectrum. This background spectrum, produced by the Rayleigh scattering of sunlight along the slant column viewed by the instrument, is modified by extinction of the scattered sunlight by the OH in the same column. The "true" background can be written

$$B(\lambda) = B_0 \exp\{-\sigma(\lambda)_{OH}\eta_{OH}\},$$

where η is the effective column abundance of OH. As a result, the retrieved OH radiances described by (5) must be corrected by the amount

$$\Delta I_{OH}(\lambda, z)|_f = C_1(z) B_0[1 - \exp\{-\sigma(\lambda)_{OH}\eta(z)_{OH}\}].$$

The essential point is that the correction at each altitude depends directly on the apparent brightness of the background at that altitude, $C_1(z)B_0$, so that the effect is most important at the lowest altitudes. The magnitude of the corrections and the sensitivity of the retrieved OH density profile to them were estimated for the condition of the three profiles reported by SUM97. Above 55 km the correction is less than 1% of the total observed OH radiance but at 50 km the value is 2.2 ± 0.4% which results in an increase in the inferred OH density at 50 km of about 7%. Although, in principal, the correction should be computed iteratively within the inversion algorithm (as is OH self-absorption), in view of the fact that the corrections are small, the results reported below were corrected by a single iteration. The sensitivity of the retrievals in the upper stratosphere will be somewhat larger and will be rigorously evaluated in a future publication devoted to the data for that region.

6.3. OH Retrieval Sensitivity to Ozone

As discussed in section 5, the inversion uses an O_3 profile to compute the extinction of the solar beam and of the scattered radiation between the scattering volume and the instrument. *Summers et al.* [1996] and SUM97 describe the long-standing discrepancy between model predictions and observation of O_3 in the upper stratosphere and mesosphere. Our choice of the profile used in the inversion was based on the comparison shown in Figure 4 of SUM97. That figure compares model O_3 results at 50 km with contemporaneous measurements of CRISTA and HALOE during MAHRSI orbit 27. The comparison shows that the various values for 1000 LST are CRISTA 3.0 ± 0.2 ppmv, HALOE 2.7 ppmv, Model B 2.4 ppmv, and Model A 2.0 ppmv. Diurnal variation measurements of *Connor et al.* [1994] suggest that the HALOE measurements shown by SUM97 should be scaled downward by about 8% to compare them with the 1000 LST CRISTA measurements. The scaled HALOE value is 2.5 ppmv.

The present OH retrievals use the O_3 profile computed by Model B. This choice assumes an O_3 mixing ratio at 50 km of 2.4 ppmv. This value is in agreement with the scaled HALOE measurement, but the CRISTA data are 25% higher, and Model A is 17% lower. For this reason, it is instructive to show the sensitivity of the OH density profiles to changes in the O_3 profile. Figure 10 shows the response of the OH profile to a ±30% adjustment of the O_3 mixing ratio at 50 km and above. This comparison uses the O_3 profile shape computed by Model B of SUM97 but scaled uniformly with altitude. The figure shows that the retrieved OH profile changes about ±10% at 50 km. Figure 10 should be used as a reference for future revisions in the estimate of ozone at 50 km. It should also be noted that the MAHRSI OH densities shown by SUM97 were retrieved using a model profile with a mixing ratio of 2.0 ppmv at 50 km so that Model B ozone profile (used in the present inversion) is 20% larger than used for the previously reported results. This increase results in a 7% increase in the retrieved OH density at 50 km.

6.4. OH Retrieval Systematic Errors

Section 4.11 discussed the radiance measurement error budget and indicated that the random errors in the OH radiance retrievals were propagated through the inversion to estimate random uncertainties in the OH number densities. The systematic error budget for the inversion is summarized in Table

Table 3. Systematic Error Budget for OH Densities

Uncertainty Contributions	$+\varepsilon$, %	$-\varepsilon$, %
Estimated calibration accuracy at 308 nm	1.8	7.2
g factor calculation		
OH A–X (0, 0) band strength	5	5
Absolute solar irradiance	2	2
OH (0, 0) atmospheric opacity correction	2	2
Solar spectrum wavelength	3	4
Total of altitude independent errors	13.8	20.2
Quenching of $v' = 0$ level at 50 km	6	6
OH background extinction at 50 km	1	1
Vibrational energy transfer to $v' = 0$ level at 50 km	0	4
Ozone, assuming a ±30% abundance uncertainty		
at 50 km	10	10
at 60 km	0	0

3. It includes the uncertainties in four major components: (1) the responsivity calibration discussed in section 4.5, (2) the g factor calculation, (3) the collisional deactivation rates, and (4) the "true" ozone extinction. The first two are nearly independent of altitude, while the others are strongly altitude dependent. The g factor errors are derived from published errors in the OH A–X (0, 0) band strength, the absolute solar irradiance at the top of the atmosphere, the wavelength scale of the solar irradiance, the OH (0, 0) atmospheric opacity correction applied to the solar irradiance, and the daily Doppler shift of the solar spectrum from the terminator to local noon. As can be seen from Figure 9, quenching of the $v' = 0$ level becomes much more important at lower altitudes, and Table 3 presents the values for 50 km. The uncertainties in the quenching rates depend on N value and on the collider molecule [*Copeland et al*., 1985]. A detailed study showed the contribution to the systematic error is ±6%. As discussed in section 6.1, the uncertainty in the effect of vibrational energy transfer is at most +4% and peaks near 50 km. The uncertainty in the densities due to the estimate of the correction of the background discussed in section 6.2 is about ±1% at 50 km. The uncertainty in the ozone abundance in the upper stratosphere was discussed in section 6.3. Table 3 presents the 50 km errors shown in Figure 10, but it should be noted that ozone has no effect at 60 km and above.

6.5. OH Measurement Sensitivity

This section addresses the question, How sensitive is the inversion of the ultraviolet fluorescence measurements to structure in the OH density profile in the mesosphere and in the upper stratosphere? This question is not only one of numerical inversion technique, but also considers the basic physics of the measurement. For example, given the combination of ozone absorption and collisional quenching at lower altitudes, how precisely can the experiment measure the OH density at 50 km?

6.5.1. Mesosphere. As mentioned in section 5.2, the inversion was not constrained by any a priori profile because there exists no global climatology of observed OH distribution in the middle atmosphere. Thus only the smoothness of the retrieved density profile is constrained, while its shape is determined by the observed radiance. Although the random errors are propagated through the inversion as an estimate of the ability of the measurement to resolve features in the vertical distribution, it is also useful to compare the forward calculation of radiance profiles based on 1-D model OH densities with the magnitude and uncertainty of the observed profiles for the same conditions.

Figure 2 of SUM97 compares model calculations of vertical OH density profiles for three different local time-latitude combinations with the corresponding profiles retrieved from 18 different orbits. In Figure 11a we show the same six model profiles compared with the averages of those 18 orbits. Figure 11b compares radiance profiles computed from these models to the averaged observed radiance profiles from which the OH densities were retrieved. These model calculations are presented here to demonstrate that the discrepancies between model and observed OH are not only apparent in the OH density profiles but also that predicted radiances are easily distinguished from the observed radiances, and that the differences are well outside the random measurement error. That is, the model-data differences are not an artifact of the inversion.

6.5.2. Upper stratosphere. The Rayleigh-scattering limb radiance profile increases at lower altitudes with the scale height of the background atmosphere until about 42 km where ozone and Rayleigh extinction limit its growth and result in a peak value. At the same time, OH self-absorption, ozone extinction, and collisional quenching combine to diminish the apparent OH radiance for a given OH density at tangent heights below 60 km. As a result, the measured OH radiance in the upper stratosphere is about 2–5% of the total signal, and that radiance includes large foreground contributions from the mesospheric column. Although the OH spectra retrieved at 50 km and below are of high quality (Plate 3), there may be a concern that the measurement random error is so large that the retrieval returns number densities at the tangent point with large oscillations that obscure the true value. Figure 12 shows the results of a calculation which addresses these issues. The solid curve shows the radiance profile measured at 10°N latitude and 0930 LST for orbit 27 together with the measurement random error. The dashed curves are the result of a forward calculation for a model density profile scaled to fit the data at 65 km and above, but below 65 is scaled by linear functions which are each 1.0 at 65 km, but one of which smoothly decreases to 0.5, and one increases to 1.5 at 50 km. Thus the model densities are forced to smoothly decrease or increase by 50% below 65 km. The figure shows that the 50% density decrease at 50 km resulted in a 25% decrease in total OH radiance, and similarly that 50% density increase produced a 24% radiance increase. The random error at 50 km is about 6%. Thus the experiment is easily able to measure a 50% variation at the stratopause.

6.6. NO Measurement Sensitivity

Stevens et al. [1997] reported the results of the 1994 NO observations. The number density profiles inferred from the data contain remarkable vertical structures which were found to be comparable to similar structures observed by the HALOE experiment. Although Stevens et al. showed that the amplitude of the inferred layers in the NO profile exceeded the propagated random errors of the measurements, it is also useful to compare the observed radiance profile with a forward model calculation to better illustrate the relative uncertainties. The left-hand panel of Figure 13 compares the density profile observed at 52°N latitude on orbit 51, with a synthetic, smoothly varying layer having the same vertical column abundance as the retrieved profile. The right-hand panel shows the

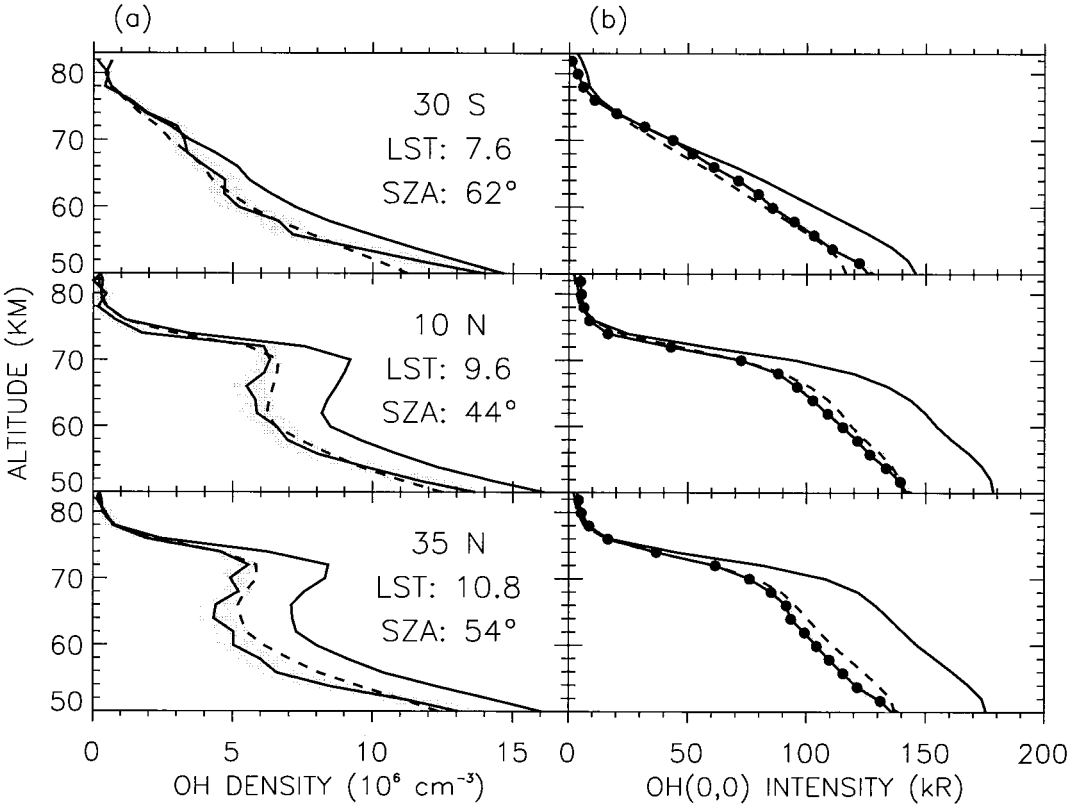

Figure 11. Model-data comparisons for OH (a) density and (b) radiance profiles for three local times and latitudes. The data are the average of 18 orbits of observations, and the models are from SUM97. The shaded region indicates the 1σ random error of the measurements. The radiances are the totals of the 11 features observed by MAHRSI.

corresponding observed and calculated radiance profiles. The shaded envelope shows the random error of the measurement in both panels. The comparison shows clearly that departures from a smooth density profile are several times the random error.

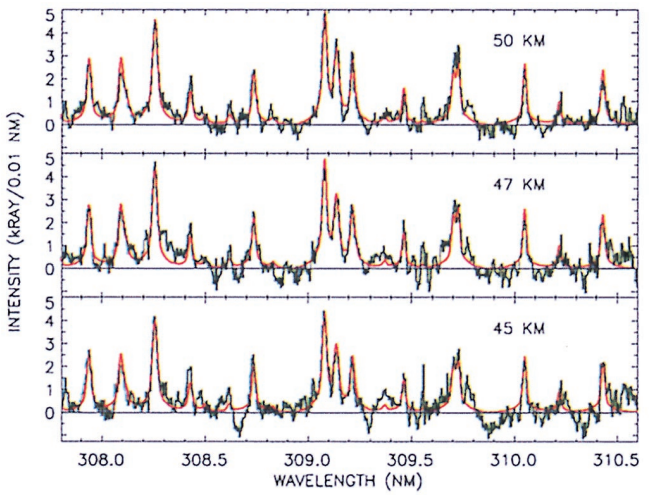

Plate 3. OH fluorescence spectra from the upper stratosphere. The increase in random noise at lower altitudes is due to the relative increase in brightness of the Rayleigh background. The local solar time for these data is 0900, and the SZA is 45°.

6.7. OH Diurnal Variation

The MAHRSI observations provide unique insight into the behavior of HO_x chemistry in the mesosphere and upper

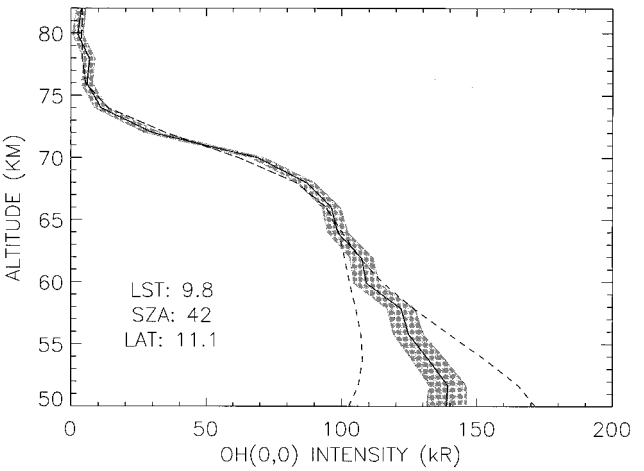

Figure 12. Sensitivity of the inversion to changes in OH densities at the stratopause compared with the random error in the measured OH radiance profile. The standard model profile was scaled by ±50% at the stratopause but kept constant above 65 km. The figure shows that changes of 50% in the density produce radiance changes several times the random error. The radiances are the totals of the 11 features observed by MAHRSI.

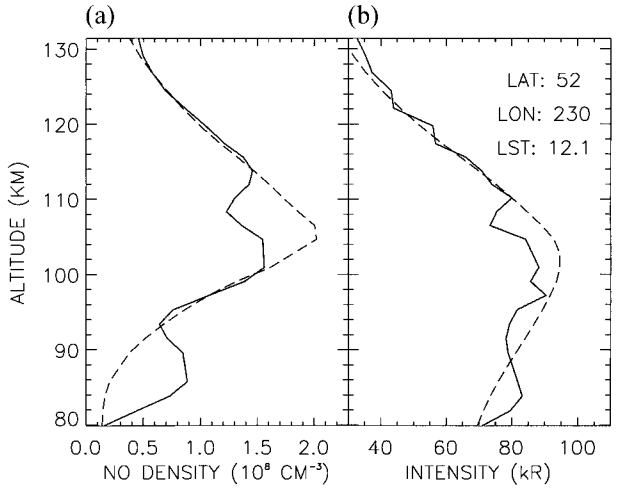

Figure 13. Model data comparisons for NO (a) density and (b) radiance for 50°N latitude from orbit 51. The shaded regions indicate the 1σ random error of the measurements.

stratosphere with changes in LST and SZA. However, because of the orbital lighting conditions, specific local solar times are confined to specific latitude regions so that latitudinal variations are not resolved from local time variations. Figure 14 illustrates the observed diurnal variation of the OH vertical profile. The individual profiles are averages of limb scans with ±15 min of the local times 0740, 0840, 0940, and 1040 from 18 orbits. The changing shape of the profile as the mesospheric layer forms is clearly seen. This is seen with much higher time resolution in Figure 15 which shows a scatterplot of the data from the same set of orbits and portrays the variation with LST of the number density at the altitudes of 50, 60, and 70 km. It should be noted that the sunrise pulse of OH observed during the Stratospheric Photochemistry, Aerosols, and Dynamics Expedition (SPADE) aircraft campaign [*Salawitch et al*., 1994] is not apparent in the mesospheric data.

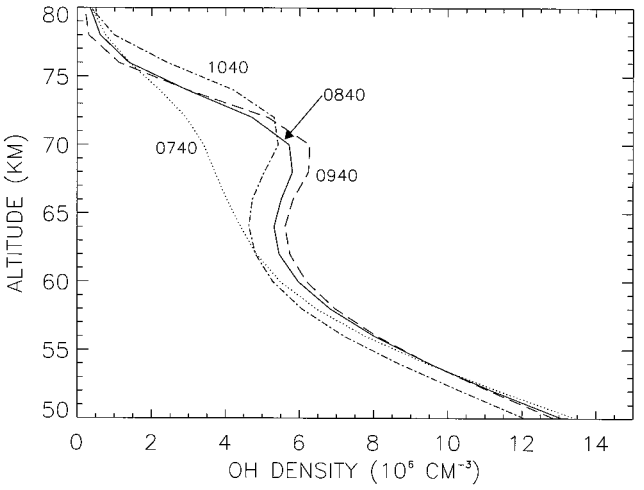

Figure 14. Observed diurnal variation of the OH density profile from 0740 through 1040 LST. Each profile is the average of limb scans from 18 orbits of data which are within ±15 min in local time on November 5–6, 1994.

6.8. OH Geographic Variation

As discussed by SUM97, the HALOE instrument on the UARS satellite observed a narrow layer of enhanced H_2O mixing ratios which peaked near 65 km with zonally averaged values as large as 8 ppmv during the period from October 23 to November 30, 1994, which includes the MAHRSI flight. Agreement between the model predictions of the shape of the mesospheric profile was not achieved until the HALOE profile was used in the 1-D model calculations. Furthermore, SUM97 showed the striking similarity in the latitudinal distribution of the two data sets for the altitudes between 65 and 75 km. Together, these comparisons show correlation between the two measurements in altitude and latitude. A search for horizontal correlation led to further examination of the HALOE measurements and revealed that the high-altitude tip (above 72 km) of the mesospheric layer between 20° and 35°N latitude was in fact confined to the region between 60°E and 70°W longitude. Plate 4 shows the average OH density between 72 and 80 km measured by MAHRSI during orbits 55–70. This figure shows that the OH measurements also show considerable geographic variation in the same region. The red disks indicate the location of individual HALOE scans contemporaneous with the MAHRSI measurements. The results of the two experiments are compared in Figure 16. The correlation between the measurements provides the third spatial dimension of corroborating evidence for the existence of an H_2O layer that cannot be predicted by the conventional theory of the photochemistry and transport H_2O through the middle atmosphere (SUM97).

7. Summary

The MAHRSI ultraviolet spectrograph experiment operated successfully for 185 hours during the November 1994 flight of the CRISTA-SPAS satellite. During 75 orbits, MAHRSI acquired 1100 daytime limb scans of the solar resonance fluorescence OH A (0, 0) band in the wavelength region near 308 nm. During 48 hours, 818 limb scans of the fluorescence NO γ (1, 0) band at 215 nm were obtained. The projected height of the field of view at the tangent point was 300 m for a tangent height of 68 km. The random error in the retrieved number

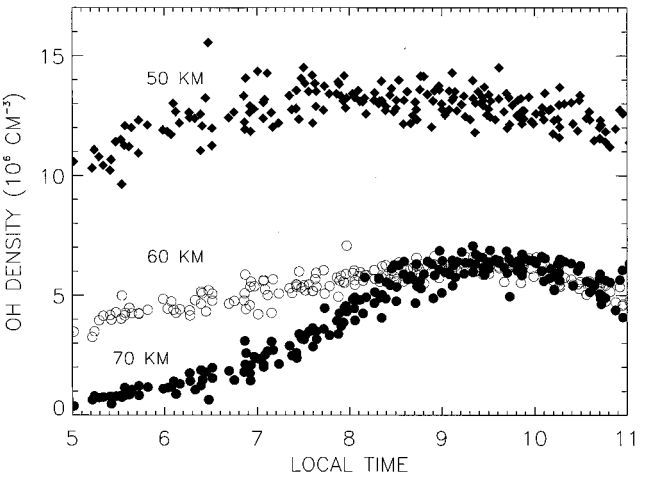

Figure 15. Observed local time dependence of the OH density at 50, 60, and 70 km for morning and afternoon. Data are from same limb scans as Figure 17.

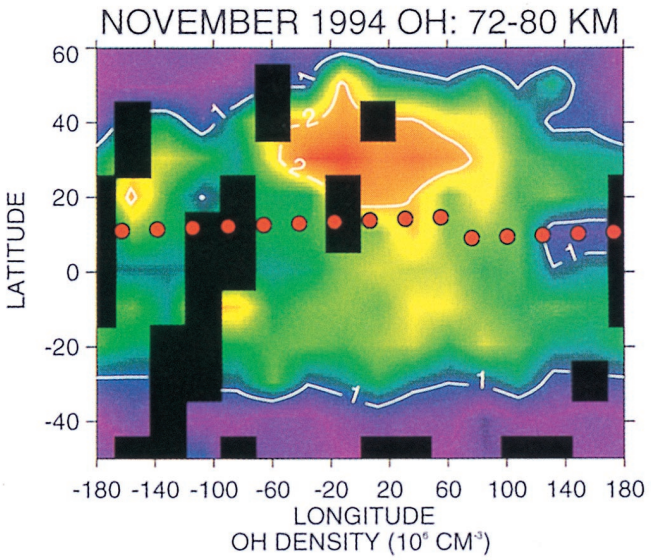

Plate 4. Observed geographic distribution of the OH column above 72 km showing the region of enhanced OH. The red disks indicate the location of contemporaneous measurements of H_2O in the same altitude region by HALOE. Data are from limb scans on November 7–8, 1994.

density profiles is dominated by photon shot noise and is typically better than 5–10% but depends on local solar time, solar zenith angle, and altitude. The OH data extend from 52°S to 62°N latitude and provide the first global maps of the distribution of OH in the mesosphere and upper stratosphere. The NO data include a unique 7.5 hour snapshot which reveals an NO distribution between altitudes 140 and 80 km that is highly structured and variable, both vertically and horizontally over the same latitude region.

This paper has presented a detailed description of the experiment, described the calibration and characterization of the instrument, and addressed several issues relevant to the reduction and inversion of the OH data. Finally, new results are presented that show good correlation in altitude, latitude, and longitude between the shape of a pronounced layer of OH at a height of 70 km with the observations of a mesospheric H_2O layer observed during the flight by the HALOE instrument on the UARS satellite.

MAHRSI was successfully flown for a second time in August 1997 under conditions that extended the geographical coverage to 72°N latitude and local solar time coverage through the afternoon hours. The results of that flight and a detailed model-data comparison of the NO observations from both flights will be presented in future publications.

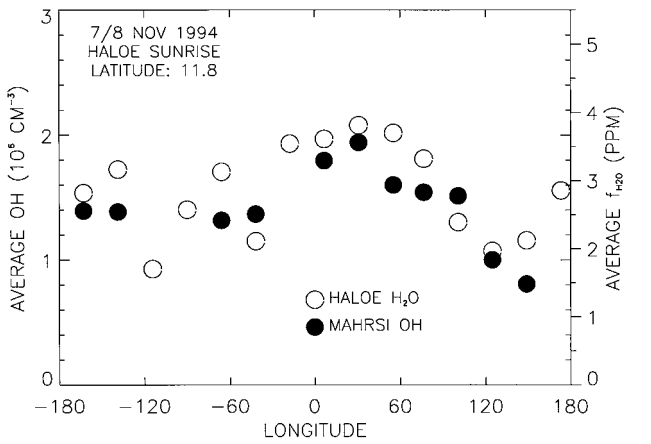

Figure 16. MAHRSI OH number density measurements averaged over the 72–80 km region compared with the contemporaneous H_2O mixing ratio measurements averaged over the same region and made during the same time period.

Acknowledgments. The successful flight of MAHRSI was made possible by the dedicated efforts of R. Feldman, J. Moser, W. Sawchuck, L. Grove, R. Dekema, T. Seeley, G. Carruthers, L. Marlin, K.-W. Li, A. Kenig, K. Moritz, and the ASTRO-SPAS team at Daimler-Benz Aerospace AG, and the flight crew of the STS-66 space shuttle mission. J. Morrill contributed to many aspects of the MAHRSI project, and D. Prinz wrote the optical ray tracing code used to develop the instrument. We thank M. Summers and D. Siskind for many helpful discussions, J.-H. Yee for his suggestions regarding the radiance retrieval, R. Copeland for his comments on the VET measurements, and R. Meier for his careful reading and comments on the manuscript. The Office of Naval Research, the U.S. Air Force Space Test Program, and the ARSAP component of the Strategic Environmental Research and Development Program supported this work.

References

Anderson, J. G., Rocket measurements of OH in the mesosphere, *J. Geophys. Res.*, *76*, 7820–7825, 1971.

Bass, A. M., and R. J. Paur, The ultraviolet cross-sections of ozone, I, Measurements in atmospheric ozone, in *Proceeding of the Quadrennial Ozone Symposium in Halkidiki, Greece*, edited by C. Zerefos and A. Ghazi, pp. 606–616, D. Reidel, Norwell, Mass., 1985.

Bates, D. R., and M. Nicolet, The photochemistry of atmospheric water vapor, *J. Geophys. Res.*, *55*, 301, 1950.

Brune, W. H., et al., Airborne in-situ OH and HO2 observations in the cloud-free troposphere and lower stratosphere during SUCCESS, *Geophys. Res. Lett.*, *25*, 1701–1704, 1998.

Carli, B., M. Carlotti, B. M. Dinelli, F. Mencaraglia, and J. H. Park, The mixing ratio of the stratospheric hydroxyl radical from far infrared emission measurements, *J. Geophys. Res.*, *94*, 11,049–11,058, 1989.

Cohen, R. C., et al., Are models of catalytic removal of O_3 and HO_x accurate? Constraints from in situ measurements of the OH and HO_2 ratio, *Geophys. Res. Lett.*, *21*, 2539–2542, 1994.

Connor, B. J., D. E. Siskind, J. J. Tsou, A. Parrish, and E. E. Remsberg, Ground-based microwave observations of ozone in the upper stratosphere and mesosphere, *J. Geophys. Res.*, *99*, 16,757–16,770, 1994.

Conway, R. R., M. H. Stevens, J. G. Cardon, S. E. Zasadil, C. M. Brown, J. S. Morrill, and G. H. Mount, Satellite measurements of hydroxyl in the mesosphere, *Geophys. Res. Lett.*, *23*, 2093–2096, 1996.

Copeland, R. A., M. J. Dyer, and D. R. Crosley, Rotational-level-dependent quenching of $A^2\Sigma^+$ OH and OD, *J. Chem. Phys.*, *82*, 4022–4032, 1985.

Grainger, J. F., and J. Ring, Anomalous Fraunhofer line profiles, *Nature*, *193*, 493, 1962.

Heaps, W. S., and T. J. McGee, Progress in stratospheric hydroxyl measurements by balloon-borne LIDAR, *J. Geophys. Res.*, *90*, 7913–7921, 1985.

Hedin, A. E., Extension of the MSIS thermosphere model into the middle and lower atmosphere, *J. Geophys. Res.*, *96*, 1159–1172, 1991.

Hilsenrath, E., D. E. Williams, R. T. Caffrey, R. P. Cebula, and S. J. Hynes, Calibration and radiometric stability of the Shuttle Solar Backscatter Ultraviolet (SSBUV) experiment, *Metrologia*, *30*, 243–248, 1993.

Janz, S., E. Hilsenrath, J. Butler, D. F. Heath, and R. P. Cebula, Uncertainties in radiance calibrations of Backscatter Ultraviolet (BUV) instruments, *Metrologia*, *32*, 637–641, 1996.

Johnson, D. G., K. W. Jucks, W. A. Traub, and K. V. Chance, Smithsonian stratospheric far-infrared spectrometer and data reduction system, *J. Geophys. Res.*, *100*, 3091–3106, 1995.

Kudo, K., T. Arai, and T. Ogawa, Method for determining the degrees

of polarization of infrared polarizers and monochromators, *J. Opt. Soc. Am*., *60*, 1046, 1969.

Kurucz, R., I. Furenlid, J. Brault, and L. Testerman, *National Solar Observatory Atlas*, vol. 1, Harvard Univ. Press, Cambridge, Mass., 1984.

Morgan, M. F., D. G. Torr, and M. R. Torr, Preliminary measurements of mesospheric OH $X^2\Pi$ by ISO on ATLAS 1, *Geophys. Res. Lett*., *20*, 511–514, 1993.

Mount, G. H., and E. Williams, An overview of the tropospheric OH photochemistry experiment, Fritz Peak, Colorado, fall 1993, *J. Geophys. Res*., *102*, 6171–6186, 1997.

Offermann, D., and R. R. Conway, Mission studies the composition of Earth's middle atmosphere, *Eos Trans. AGU*, *76*, 337–342, 1995.

Offermann, D., K. U. Grossmann, P. Barthol, P. Knieling, M. Riese, and R. Trant, Cryogenic Infrared Spectrometers and Telescopes for the Atmosphere (CRISTA) experiment and middle atmosphere variability, *J. Geophys. Res*., this issue.

Pickett, H. M., and D. B. Peterson, Comparison of measured stratospheric OH with predictions, *J. Geophys. Res*., *101*, 16,789–16,796, 1996.

Reader, J., Optimizing Czerny-Turner spectrographs: A comparison between analytic theory and ray tracing, *J. Opt. Soc. Am*., *59*, 1189–1196, 1969.

Rodgers, C. D., Characterization and error analysis of profiles retrieved from remote sounding measurements, *J. Geophys. Res*., *95*, 5587–5595, 1990.

Russell, J. M., III, et al., The Halogen Occultation Experiment, *J. Geophys. Res*., *98*, 10,777–10,797, 1993.

Salawitch, R. J., et al., The diurnal variation of hydrogen, nitrogen, and chlorine radicals: Implication for the heterogeneous production of HNO_2, *Geophys. Res. Lett*., *21*, 2551–2554, 1994.

Siskind, D. E., and D. W. Rusch, Nitric oxide in the middle and upper thermosphere, *J. Geophys. Res*., *97*, 3209–3217, 1992.

Siskind, D. E., C. A. Barth, and J. M. Russell III, A climatology of nitric oxide in the mesosphere and thermosphere, *Adv. Space Res*., *21*, 1353–1362, 1998.

Stevens, M. H., Nitric oxide γ band fluorescent scattering and self-absorption in the mesosphere and lower thermosphere, *J. Geophys. Res*., *100*, 14,735–14,742, 1995.

Stevens, M. H., and R. R. Conway, Calculated OH $A^2\Sigma^+$–$X^2\Pi$ (0, 0) band rotational emission rate factors for solar resonance fluorescence, *J. Geophys. Res*., this issue.

Stevens, M. H., R. R. Conway, J. G. Cardon, and J. M. Russell III, MAHRSI observations of nitric oxide in the mesosphere and lower thermosphere, *Geophys. Res. Lett*., *24*, 3213–3216, 1997.

Stimpfle, R. M., and J. G. Anderson, In situ detection of OH in the lower stratosphere with a balloon-borne high repetition rate laser system, *Geophys. Res. Lett*., *15*, 1503–1506, 1988.

Stimpfle, R. M., P. O. Wennberg, L. B. Lapson, and J. G. Anderson, Simultaneous, in situ measurements of OH and HO_2 in the stratosphere, *Geophys. Res. Lett*., *17*, 1905–1908, 1990.

Summers, M. E., R. R. Conway, D. E. Siskind, D. F. Strobel, and S. E. Zasadil, Mesospheric HO_x photochemistry: Constraints from concurrent measurements of OH and H_2O, *Geophys. Res. Lett*., *23*, 2096–2100, 1996.

Summers, M. E., et al., Implications of satellite OH observations for middle atmospheric H_2O and ozone, *Science*, *277*, 1967–1970, 1997.

Thompson, A. M., The oxidizing capacity of the Earth's atmosphere: Probable past and future changes, *Science*, *256*, 1157–1165, 1992.

Titz, R., M. Birk, D. Hausamann, R. Nitsche, F. Schrier, J. Urban, H. Kuellmann, and H. P. Roeser, Observations of stratospheric OH at 2.5 THz with an airborne heterodyne system, *Infrared Phys. Technol*., *36*, 883–891, 1995.

Twomey, S., On the numerical solution of Fredholm integral equations of the first kind by the inversion of the linear system produced by quadrature, *J. Assoc. Comput. Mach*., *10*, 97–101, 1963.

Twomey, S., The application of numerical filtering to the solution of integral equations encountered in indirect sensing measurements, *J. Franklin Inst*., *279*(2), 98–109, 1965.

Twomey, S., Comparison of constrained linear inversion and an iterative nonlinear algorithm applied to the indirect estimation of particle size distributions, *J. Comput. Phys*., *18*, 188–200, 1975.

Twomey, S., *Introduction to Mathematics of Inversion in Remote Sensing and Indirect Measurements*, Elsevier, New York, 1977.

Waters, J. W., Atmospheric measurements by the MLS experiments: Results from UARS and plans for the future, *Adv. Space Res*., *21*, 1363–1372, 1998.

Wennberg, P. O., et al., Removal of stratospheric O_3 by radicals: In situ measurements of OH, HO_2, NO, NO_2, ClO, and BrO, *Science*, *266*, 398–403, 1994a.

Wennberg, P. O., et al., Aircraft-borne, laser-induced fluorescence instrument for the in situ detection of hydroxyl and hydroperoxyl radicals, *Rev. Sci. Instrum*., *65*, 1858–1876, 1994b.

Williams, L. R., and D. R. Crosley, Collisional vibrational energy transfer of OH($A^2\Sigma^+$, $v' = 1$), *J. Chem. Phys*., *104*, 6507, 1996.

Wood, S. W., D. J. Keep, C. R. Burnett, and E. B. Burnett, Column abundance measurements of atmospheric hydroxyl at 45°S, *Geophys. Res. Lett*., *21*, 1607–1610, 1994.

C. M. Brown, R. R. Conway, and M. H. Stevens, E. O. Hulburt Center for Space Research, Naval Research Laboratory, Washington, DC 20375. (e-mail: conway@map.nrl.navy.mil)

J. G. Cardon, Computational Physics, Inc., 2750 Prosperity Ave., Suite 600, Fairfax, VA 22031.

G. H. Mount, Department of Civil and Environmental Engineering, Washington State University, Pullman, WA 99163.

S. E. Zasadil, Union Switch & Signal, Inc., 1000 Technology Dr., Pittsburgh, PA 15227.

(Received June 11, 1998; revised September 22, 1998;
accepted September 24, 1998.)